

# Multifractal Analysis of Multivariate Images Using Gamma Markov Random Field Priors\*

Herwig Wendt<sup>†</sup>, Sébastien Combrexelle<sup>†</sup>, Yoann Altmann<sup>‡</sup>, Jean-Yves Tourneret<sup>†</sup>, Stephen McLaughlin<sup>‡</sup>, and Patrice Abry<sup>§</sup>

**Abstract.** Texture characterization of natural images using the mathematical framework of multifractal (MF) analysis, enables the study of the fluctuations in the regularity of image intensity. Although successfully applied in various contexts, the use of MF analysis has so far been limited to the independent analysis of a single image, while the data available in applications are increasingly multivariate. This paper addresses this limitation and proposes a joint Bayesian model and associated estimation procedure for MF parameters of multivariate images. It builds on a recently introduced generic statistical model that enabled the Bayesian estimation of MF parameters for a single image and relies on the following original key contributions: First, we develop a novel Fourier domain statistical model for a single image that permits the use of a likelihood that is separable in the MF parameters via data augmentation. Second, a joint Bayesian model for multivariate images is formulated in which prior models based on gamma Markov random fields encode the assumption of the smooth evolution of MF parameters between the image components. The design of the likelihood and of conjugate prior models is such that exploitation of the conjugacy between the likelihood and prior models enables an efficient estimation procedure that can handle a large number of data components. Numerical simulations conducted using sequences of multifractal images demonstrate that the proposed procedure significantly outperforms previous univariate benchmark formulations at a competitive computational cost.

**Key words.** Texture Analysis, Multifractal Analysis, Multivariate Images, Wavelet Leaders, Bayesian Estimation, Gamma Markov Random Field

**AMS subject classifications.** 65T60, 62H12, 62M40, 68U10, 62H35, 62F15, 62L20

## 1. Introduction.

**1.1. Context.** Texture is a perceptual attribute and different paradigms have been proposed in the literature for its characterization [24]. There is a growing body of work suggesting that a large class of natural images are modelled well by scale invariant processes [10, 55, 61], motivating the use of random fractals, scale invariance or self-similarity to characterize texture. These concepts can be linked to the degree of point-wise singular behavior or *regularity* (smoothness) of the image amplitude [37, 44]. From this point of view, texture models can

---

\*Submitted to the editors 6 October 2017.

**Funding:** Work supported by Grant ANR-16-CE33-0020 MultiFracs and Grant ANR-12-BS03-003 Hypanema. S. Combrexelle was supported by the Direction Générale de l'Armement (DGA) under the DGA/DSTL collaborative PhD programme. S. McLaughlin acknowledges the support of EPSRC grant number EP/J015180/1 and the supply of the hyperspectral image data from DSTL.

<sup>†</sup>IRIT-INPT, CNRS, University of Toulouse, France ([herwig.wendt@irit.fr](mailto:herwig.wendt@irit.fr), [sebastien.combrexelle@gmail.com](mailto:sebastien.combrexelle@gmail.com), [jean-yves.tourneret@enseiht.fr](mailto:jean-yves.tourneret@enseiht.fr)).

<sup>‡</sup>School of Engineering and Physical Sciences, Heriot-Watt University, Edinburgh, UK ([y.altmann@hw.ac.uk](mailto:y.altmann@hw.ac.uk), [s.mclaughlin@hw.ac.uk](mailto:s.mclaughlin@hw.ac.uk)).

<sup>§</sup>Laboratoire de Physique, Université de Lyon, ENS de Lyon, Université Claude Bernard, CNRS, F-69342 Lyon, France ([patrice.abry@ens-lyon.fr](mailto:patrice.abry@ens-lyon.fr)).

33 be seen as densely interwoven sets of singularities of different regularity strengths, commonly  
 34 measured by the Hölder exponent  $h$  [26, 44]. The suitable mathematical framework for the  
 35 study of these models is *multifractal analysis* (MFA) [4, 32], which enables scale invariant  
 36 image texture to be described via the spatial fluctuations of the point-wise regularity expo-  
 37 nents of the image. More precisely, it provides a global characterization of the texture via  
 38 the so-called *multifractal spectrum*  $D(h)$ , collecting the Hausdorff dimensions of the sets of  
 39 positions that share the same regularity exponent. This paper is focused on one of the cen-  
 40 tral parameters in MFA, the *multifractality* or *intermittency* parameter  $c_2$ , which is related  
 41 to the width of the multifractal spectrum (hence, to the degree of fluctuations of regularity  
 42 exponents in the image). It enables discrimination between the two major classes of scale  
 43 invariant processes used in applications: (additive construction-based) self-similar processes  
 44 for which  $c_2 = 0$ , and (multiplicative construction-based) processes constructed from multi-  
 45 fractal multiplicative cascade (MMC) for which  $c_2$  is strictly negative [56]. The parameter  $c_2$   
 46 therefore highlights departures from Gaussian marginals as well as changes in the local tran-  
 47 sient dependence structure of texture. The corresponding practical analysis tools rely on the  
 48 scale dependence of the statistics of certain multi-resolution quantities (such as increments,  
 49 wavelet coefficients or, more recently, wavelet leaders [26], which will be used here). The main  
 50 concepts of multifractal analysis are briefly recalled in Section 2, cf. [26, 27, 44] for details.

51 **1.2. Multifractal analysis of multivariate images.** MFA has been successfully used in a  
 52 number of applications including texture classification [55, 61], biomedical imaging [5, 31, 33],  
 53 physics [41, 48], biology [50], climate research [34] and art investigation [1, 13, 30]. Yet, its  
 54 application remains so far conceptually limited to the analysis of single images with homoge-  
 55 neous scale invariant properties [29]. The main reason for this resides in the definition of the  
 56 multifractal spectrum, which is intrinsically univariate. Although definitions of a multivariate  
 57 multifractal spectrum have been studied, cf., e.g., [23, 38, 49] and the recent contributions  
 58 [28, 57], these attempts remain essentially limited to pairs of time series and are of little rel-  
 59 evance for  $M$ -tuples of data for  $M \gg 2$ . This limitation has become increasingly urgent in  
 60 view of the number of recent applications in which the acquired images are *multivariate*, i.e.,  
 61 they consist of a set of images (multitemporal, multispectral, multimodal, ...) or spatially  
 62 organized collections of image patches. Such data can provide a rich resource for information,  
 63 on condition that they are analyzed *jointly* rather than individually [42].

64 **1.3. Related work: Estimation of  $c_2$ .** The current existing estimation procedures for the  
 65 multifractality parameter are limited to the independent processing of individual images. The  
 66 standard estimator for  $c_2$  is based on a simple linear regression of the sample variance of the  
 67 logarithm of suitable multiresolution quantities over several analysis scales [9] (cf., (5)). This  
 68 estimator is appealing for its simplicity and low computational cost, yet it has been reported  
 69 to suffer from poor performance when applied to small-sized images [58]. A related approach,  
 70 based on a wavelet scattering transform, was recently studied in [8]. Several parametric  
 71 model-based approaches have also been proposed. These include maximum likelihood methods  
 72 [6, 11, 39, 60] and the generalized method of moments [35]. Yet, their definitions are tied  
 73 to specific instances of self-similar or multifractal processes and the use of fully parametric  
 74 models is often too restrictive in practice. More recently, a Bayesian estimation framework  
 75 was studied in [17]. It relied on a flexible semi-parametric model for the statistics of the

76 logarithm of wavelet leaders that is generically valid for self-similar and MMC processes.  
77 This model showed excellent estimation performance. However, its high computational cost  
78 made it difficult to apply to the analysis of multivariate data, and a first attempt at its direct  
79 application with a simultaneous autoregressive smoothing prior was reported in [18]. However,  
80 it was limited to the analysis of small image sequences for this reason.

81 **1.4. Goals and contributions.** The goal of the present work is to go beyond these ex-  
82 isting, inherently univariate, estimation procedures for  $c_2$  and propose the first operational  
83 approach for the multifractal analysis of multivariate images. Specifically, we propose to con-  
84 duct the analysis within a multivariate Bayesian model that *jointly* describes the collection of  
85 multifractality parameters  $c_2$  associated with the multifractal spectra of different individual  
86 data components. This Bayesian multivariate estimation framework builds upon ingredients  
87 of the model proposed in [17], which is recalled in Section 3.1. However, it also presents some  
88 essential new characteristics relying on the following two main contributions.

89 First, a novel Fourier domain statistical model for log-leaders is proposed. This model  
90 allows conjugate inverse-gamma ( $\mathcal{IG}$ ) prior distributions to be defined. Consequently, it leads  
91 to efficient inference procedures that are appropriate for multivariate data. It dwells on three  
92 original key ingredients, described in Section 3.2: 1) The Whittle approximation [6, 53] is  
93 used to build an original Gaussian model for the Fourier coefficients of log-leaders of MMC  
94 processes, 2) The implicit joint constraint on the multifractal parameters is decomposed into  
95 independent positivity constraints through a suitable reparametrization, 3) Data augmen-  
96 tation is used in order to define an augmented distribution whose parameters are easier to  
97 estimate.

98 Second, we use this novel model in the formulation of a joint Bayesian model for mul-  
99 tivariate images (cf. Section 4). Specifically, we propose to encode the prior belief that the  
100 multifractality parameter evolves slowly across time or spectral bands (for sequence of images)  
101 or throughout space (for image patches) through the design of a gamma Markov random field  
102 (GaMRF) prior. This GaMRF prior induces positive correlation between the multifractality  
103 parameters associated with different image components and hence regularizes estimation. This  
104 leads to simple conditional distributions for the parameters of the augmented Fourier domain  
105 model, namely  $\mathcal{IG}$  distributions. As a result, the inference of the parameters of the associated  
106 posterior distribution (described in Section 5) can be conducted by a Gibbs sampler whose  
107 steps do not require accept-reject moves, leading to an efficient estimation procedure adapted  
108 to a large number of unknowns. This estimation framework elaborates on the approach  
109 described in [16], which was limited to the local estimation of  $c_2$  in that it applied only to  
110 non-overlapping image patches and could be applied to a single image one at a time, two  
111 significant restrictions when application to real-world data is envisaged, as is the case here.

112 The performance of the method is assessed numerically in Section 6 using sequences of syn-  
113 thetic multifractal images with piece-wise constant (in time and space) multifractal properties.  
114 The proposed joint estimator yields significantly improved estimation performance compared  
115 to previous univariate formulations with a competitive computational cost (root-mean-squared  
116 error values are more than one order of magnitude smaller than those of standard linear re-  
117 gression, with a 4 times larger computational cost). Finally, Section 7 illustrates the benefits  
118 of the proposed procedure for the analysis of real-world data *via* two applications devoted to

119 hyperspectral and multitemporal imaging. Supplementary 3D animations associated with the  
 120 results obtained in Sections 6 and 7, as well as MATLAB codes, are available online (see [14]).

## 121 2. Multifractal Analysis of images.

122 **2.1. Local regularity and multifractal spectrum.** Denote as  $X(\mathbf{y}) : \mathbf{y} \in \mathbb{R}^2 \rightarrow X \in \mathbb{R}$  the  
 123 image under analysis, where  $\mathbf{y} = (y_1, y_2)$  stands for the spatial variable. The purpose of MFA  
 124 is to characterize the fluctuations of the *point-wise regularity* of the image  $X$ . This regularity  
 125 is most commonly measured using the *Hölder exponent* [26, 44], defined as follows. Assuming  
 126 that  $X$  is locally bounded<sup>1</sup>,  $X$  is said to belong to  $C^\alpha(\mathbf{y}_0)$  at position  $\mathbf{y}_0$  if there exist  $\alpha > 0$   
 127 and a polynomial  $P_{\mathbf{y}_0}$  of degree smaller than  $\alpha$  such that  $\|X(\mathbf{y}) - P_{\mathbf{y}_0}(\mathbf{y})\| \leq C\|\mathbf{y} - \mathbf{y}_0\|^\alpha$  for  $\mathbf{y}$   
 128 sufficiently close to  $\mathbf{y}_0$ , with  $\|\cdot\|$  denoting the Euclidian norm. The Hölder exponent is then  
 129 defined as

$$130 \quad (1) \quad h(\mathbf{y}_0) \triangleq \sup\{\alpha : X \in C^\alpha(\mathbf{y}_0)\}$$

132 with, qualitatively, the smaller (resp. larger)  $h(\mathbf{y}_0)$ , the rougher (resp. smoother)  $X$  at  $\mathbf{y}_0$ .  
 133 MFA provides a *global* description of the fluctuations of  $h(\mathbf{y})$  in space in terms of the *mul-*  
 134 *tifractal spectrum*  $D(h)$ . The multifractal spectrum is defined as the Hausdorff dimension of  
 135 the sets of positions  $\mathbf{y}$  that have identical Hölder exponent

$$136 \quad (2) \quad \mathcal{D}(h) \triangleq \dim_H \{\mathbf{y} : h(\mathbf{y}) = h\}.$$

137 The estimation of  $D(h)$  is the central goal of MFA (for further details on MFA see [26, 27,  
 138 44]). However, it cannot be conducted based on its formal definition (2). Instead, a so-  
 139 called *multifractal formalism* is used, which allows for the assessment of  $D(h)$  via the scale  
 140 dependence of the statistical distributions of specifically tailored multiresolution coefficients  
 141 (cf., Section 2.3 below). Several different multifractal formalisms have been proposed in the  
 142 literature, relying on different multiresolution quantities, cf., e.g., [4, 26, 33, 48]. In this work,  
 143 we make use of *wavelet leaders* which have been proven to possess the key theoretical properties  
 144 for multifractal analysis purposes and have resulted in the current state-of-the-art multifractal  
 145 formalism, see, e.g., [26, 27, 54].

146 **2.2. Wavelet leaders.** The 2D gray level digitized image  $\{X(\mathbf{k}), \mathbf{k} = (k_1, k_2), k_i = 1, \dots,$   
 147  $, N\}$  is first decomposed using a discrete wavelet transform (DWT) where a square image  
 148 is considered here without loss of generality. Let  $H_0(k)$  and  $G_0(k)$  denote the low-pass and  
 149 high-pass filters defining a 1D DWT relying on a mother wavelet  $\psi$  with  $N_\psi > 0$  vanishing  
 150 moments. A common way to obtain a 2D orthonormal DWT is to use four 2D filters  $G^{(m)}(\mathbf{k})$ ,  
 151  $m = 0, \dots, 3$  defined as the tensor products of  $H_0(k)$  and  $G_0(k)$ . The 2D low-pass filter is  
 152 by convention  $G^{(0)}(\mathbf{k}) \triangleq H_0(k_1)H_0(k_2)$ , while the high-pass filters are defined by  $G^{(1)}(\mathbf{k}) \triangleq$   
 153  $H_0(k_1)G_0(k_2)$ ,  $G^{(2)}(\mathbf{k}) \triangleq G_0(k_1)H_0(k_2)$  and  $G^{(3)}(\mathbf{k}) \triangleq G_0(k_1)G_0(k_2)$ . Let  $D_X^{(0)}(j = 0, \mathbf{k}) \triangleq$   
 154  $X(\mathbf{k})$ . The 2D wavelet coefficients  $D_X^{(m)}(j, \mathbf{k})$ ,  $m = 1, \dots, 3$  and approximation coefficients  
 155  $D_X^{(0)}(j, \mathbf{k})$  for the analysis scales  $j \geq 1$  are obtained by iterative convolution of  $G^{(m)}$ ,  $m =$

---

<sup>1</sup>The local boundedness condition on  $X$  is inherent to the definition of the Hölder exponent and assumed to hold and not further discussed in what follows (cf., [27, 54, 58] for details and practical procedures for assessing and circumventing this condition).

156  $0, \dots, 3$ , with the approximation coefficients  $D_X^{(0)}(j-1, \cdot)$ , followed by decimation. In the  
 157 context of MFA, it is common to use  $L^1$  normalized wavelet coefficients, i.e.,  $d_X^{(m)}(j, \mathbf{k}) \triangleq$   
 158  $2^{-j} D_X^{(m)}(j, \mathbf{k})$ ,  $m = 1, 2, 3$  [4]. For details on wavelet transforms, cf., e.g., [3, 36].

159 Denote as  $\lambda_{j, \mathbf{k}} = \{[k_1 2^j, (k_1 + 1)2^j], [k_2 2^j, (k_2 + 1)2^j]\}$  the dyadic cube of side length  $2^j$   
 160 based at  $\mathbf{k} 2^j$ , and as  $3\lambda_{j, \mathbf{k}} = \bigcup_{n_1, n_2 \in \{-1, 0, 1\}} \lambda_{j, \mathbf{k} + n_1 \mathbf{e}_1 + n_2 \mathbf{e}_2}$  the union with its eight neighbors.  
 161 The wavelet leaders are defined as the largest wavelet coefficient within this neighborhood  
 162 over all finer scales [26]

163 (3) 
$$l(j, \mathbf{k}) \triangleq \sup_{m \in \{1, 2, 3\}, \lambda' \subset 3\lambda_{j, \mathbf{k}}} |d_X^{(m)}(\lambda')|.$$

164

**2.3. Wavelet leader multifractal formalism.** It can be shown that the  $q$ th order empirical moments of wavelet leaders  $l(j, \mathbf{k})$  behave as power laws in the limit of fine scales, i.e.,

$$\frac{1}{n_j} \sum_{\mathbf{k}} l(j, \mathbf{k})^q \sim 2^{j\zeta(q)}, \quad 2^j \rightarrow 0$$

where  $n_j$  stands for the number of coefficients available at scale  $j$ . The Legendre transform of the so-named *scaling exponents*  $\zeta(q)$  in this relation can be shown to provide an upper-bound estimate for the multifractal spectrum  $D(h)$

$$\mathcal{D}(h) \leq D(h) \inf_q (2 + qh - \zeta(q)),$$

165 see, e.g., [26, 44]. In practice, the estimate  $D(h)$  is the only quantity that is accessible in a  
 166 numerically stable way and is therefore commonly conflated with the multifractal spectrum.  
 167 In the seminal contribution [9], it was moreover shown that  $\zeta(q)$  can be expressed as

168 (4) 
$$\zeta(q) = \sum_{p=1}^{\infty} c_p \frac{q^p}{p!}$$

169 where the coefficients  $c_p$ ,  $p \geq 1$ , termed *log-cumulants*, are tied to the  $p$ th cumulant  $C_p(j)$  of  
 170 the logarithm of the wavelet leaders  $l(j, \mathbf{k})$  via the relation

171 (5) 
$$C_p(j) = c_p^0 + c_p \ln 2^j.$$

172 Computing the Legendre transform of (4), the multifractal spectrum  $D(h)$  can be developed  
 173 as

174 (6) 
$$D(h) = 2 + \frac{c_2}{2!} \left( \frac{h - c_1}{c_2} \right)^2 + \frac{-c_3}{3!} \left( \frac{h - c_1}{c_2} \right)^3 + \dots$$

175

176 when  $c_2 < 0$ , cf., e.g., [58] (when  $c_2 = 0$ ,  $D(h)$  reduces to a Delta function at  $h = c_1$ ).  
 177 The leading order coefficients  $c_p$  therefore capture most of the essential information on the  
 178 multifractal properties of  $X$  and hence are often used in applications in place of the entire  
 179 function  $D(h)$  [9, 27, 54, 58].

180 Relation (5) suggests that the coefficients  $c_p$  can be estimated by linear regression of  
 181 sample cumulants of log-leaders across scales  $j$ . Specifically, for  $c_2$ , this relation underlies  
 182 the definition of the current benchmark estimator for the multifractality parameter  $c_2$ , which  
 183 consists of performing a linear regression of the sample variance, denoted by  $\widehat{\text{Var}}$ , of  $\ln l(j, \mathbf{k})$   
 184 over a range of scales  $j \in [j_1, j_2]$

$$185 \quad (7) \quad \hat{c}_2 = \frac{1}{\ln 2} \sum_{j=j_1}^{j_2} w_j \widehat{\text{Var}}[\ln l(j, \cdot)]$$

186 where  $w_j$  are suitable regression weights, cf., [54, 58].

187 **3. Data augmented Fourier domain model for log-leaders.** The estimator (7) is known  
 188 to yield poor performance (large variance) even for moderate image size and is attractive  
 189 mainly for its low complexity. A Bayesian model for a single image that addresses this lim-  
 190 itation was proposed in [17] and is recalled briefly in Section 3.1. This model leads to an  
 191 improved estimation performance, yet it is not well suited for the design of joint priors in the  
 192 analysis of multiple images. In Section 3.2, we propose a novel data augmented statistical  
 193 model in the Fourier domain for a single image that is specifically designed to be applied to  
 194 multivariate images, as explained in Section 4.

195 **3.1. Direct model.** We denote by  $\ell_j$  the vector of all log-leaders  $\ell(j, \cdot) \triangleq \ln l(j, \cdot)$  at scale  
 196  $j$  after subtraction of their average (since it does not convey any information on  $c_2$ ).

197 **3.1.1. Likelihood.** It was recently shown that the statistics of the log-leaders  $\ell_j$  for MMC-  
 198 based processes are well approximated by a multivariate Gaussian distribution whose co-  
 199 variance  $\mathcal{C}_j(\mathbf{k}, \Delta\mathbf{k}) \triangleq \text{Cov}[l(j, \mathbf{k}), l(j, \mathbf{k} + \Delta\mathbf{k})]$  is given by the radial symmetric function  
 200  $\varrho_j(\Delta\mathbf{k}; \mathbf{c}_2)$  defined as

$$201 \quad (8) \quad \mathcal{C}_j(\mathbf{k}, \Delta\mathbf{k}) \approx \varrho_j(\Delta\mathbf{k}; \mathbf{c}_2) \triangleq \begin{cases} \varrho_j^0(\|\Delta\mathbf{k}\|; \mathbf{c}_2), & \|\Delta\mathbf{k}\| \leq 3 \\ \varrho_j^1(\|\Delta\mathbf{k}\|; \mathbf{c}_2), & 3 < \|\Delta\mathbf{k}\| \end{cases}$$

and parametrized only by

$$\mathbf{c}_2 \triangleq (c_2, c_2^0)$$

202 see [17] for details. The functions  $\varrho_j^0$  and  $\varrho_j^1$  are given by  $\varrho_j^0(r; \mathbf{c}_2) \triangleq a_j \ln(1+r) + c_2^0 +$   
 203  $c_2 \ln 2^j$ , where  $a_j \triangleq (\varrho_j^1(3; \mathbf{c}_2) - c_2^0 - c_2 \ln 2^j) / \ln 4$ , and  $\varrho_j^1(r; \mathbf{c}_2) \triangleq c_2 \ln(r/r_j) \mathbb{I}_{[0, r_j]}(r)$ , where  
 204  $r_j = \lfloor \sqrt{n_j}/4 \rfloor$  ( $\lfloor \cdot \rfloor$  truncates to integer values) and  $\mathbb{I}_A$  is the indicator function of the set  $A$ ,  
 205 respectively [17]. With these assumptions, the likelihood of  $\ell_j$  is given by

$$206 \quad (9) \quad p(\ell_j | \mathbf{c}_2) \propto |\Sigma_{j, \mathbf{c}_2}|^{-\frac{1}{2}} \exp\left(-\frac{1}{2} \ell_j^T \Sigma_{j, \mathbf{c}_2}^{-1} \ell_j\right)$$

207 where the covariance matrix  $\Sigma_{j, \mathbf{c}_2}$  is defined element-wise by  $[\Sigma_{j, \mathbf{c}_2}]_{u, v} = \varrho_j(\|\mathbf{k}_u - \mathbf{k}_v\|; \mathbf{c}_2)$ ,  
 208  $|\cdot|$  denotes the determinant and  $^T$  the transpose operator. Following [17], independence is  
 209 assumed between log-leaders at different scales  $j$ , conditionally on  $\mathbf{c}_2$ . Dependence across  
 210 scales is nevertheless partially accounted for in a hierarchical fashion because the parameters  
 211  $\mathbf{c}_2$  are modeled using the relation (5), which precisely describes the evolution across scales for

212 the *distributions* of  $\ell_j$  that is imposed by the multifractal model. This assumption leads to  
 213 the following likelihood for the vector  $\ell \triangleq [\ell_{j_1}^T, \dots, \ell_{j_2}^T]^T$

$$214 \quad (10) \quad p(\ell | \mathbf{c}_2) \triangleq \prod_{j=j_1}^{j_2} p(\ell_j | \mathbf{c}_2).$$

215 To ensure that (10) is a valid likelihood, the covariance matrices  $\Sigma_{j, \mathbf{c}_2}$ ,  $j \in \{j_1, \dots, j_2\}$ , must  
 216 be positive definite. This condition implicitly defines constraints on the parameter vector  $\mathbf{c}_2$   
 217 that can be assessed only numerically.

218 **3.1.2. Whittle approximation.** The numerical evaluation of the likelihood (9) (and hence  
 219 of (10)) is problematic even for images of small size since it requires the computation of the  
 220 matrix inverses  $\Sigma_{j, \mathbf{c}_2}^{-1}$ . To bypass this difficulty, it has been proposed in [17] to approximate  
 221 (9) with the asymptotic Whittle likelihood [2, 6, 21, 59]

$$222 \quad (11) \quad p^\dagger(\ell_j | \mathbf{c}_2) = \exp \left( -\frac{1}{2} \sum_{\mathbf{m} \in J_j} \ln \phi_j(\boldsymbol{\omega}_{\mathbf{m}}; \mathbf{c}_2) \right) \exp \left( -\frac{1}{2} \sum_{\mathbf{m} \in J_j} \frac{y_j^*(\boldsymbol{\omega}_{\mathbf{m}}) y_j(\boldsymbol{\omega}_{\mathbf{m}})}{\phi_j(\boldsymbol{\omega}_{\mathbf{m}}; \mathbf{c}_2)} \right)$$

where  $y_j(\cdot)$  is the discrete Fourier transform (DFT) of  $\ell(j, \cdot)$ , i.e.,  $y_j^*(\boldsymbol{\omega}_{\mathbf{m}}) y_j(\boldsymbol{\omega}_{\mathbf{m}})$  corresponds  
 to the periodogram of  $\{\ell(j, \mathbf{k})\}$  at frequency  $\boldsymbol{\omega}_{\mathbf{m}} = 2\pi\mathbf{m}/\sqrt{n_j}$ , and  $*$  denotes the conjugation  
 operator. The summation is taken over the grid of integers  $J_j \triangleq \llbracket [(-\sqrt{n_j} - 1)/2], \dots, \sqrt{n_j} -$   
 $\llbracket \sqrt{n_j}/2 \rrbracket \setminus \{0\}^2$ , where the zero frequency is removed, making the model mean-independent.  
 Moreover,  $\phi_j(\boldsymbol{\omega}_{\mathbf{m}}; \mathbf{c}_2)$  stands for the discretized parametric spectral density associated with  
 the covariance model (8), i.e.,

$$\phi_j(\boldsymbol{\omega}_{\mathbf{m}}; \mathbf{c}_2) = \bar{\mathcal{F}}\mathcal{T}[\varrho_j(\cdot; \mathbf{c}_2)](\boldsymbol{\omega}_{\mathbf{m}}),$$

223 where  $\bar{\mathcal{F}}\mathcal{T}[\cdot]$  stands for a discretization of the continuous time Fourier transform that takes  
 224 into account aliasing. It can be shown that  $\phi_j(\boldsymbol{\omega}_{\mathbf{m}}; \mathbf{c}_2)$  is of the form

$$225 \quad (12) \quad \phi_j(\boldsymbol{\omega}_{\mathbf{m}}; \mathbf{c}_2) = c_2 h_j^{(1)}(\boldsymbol{\omega}_{\mathbf{m}}) + c_2^0 h_j^{(2)}(\boldsymbol{\omega}_{\mathbf{m}})$$

226 where the vectors  $h_j^{(1)}$  and  $h_j^{(2)}$  do not depend on the parameter vector  $\mathbf{c}_2$ . They can hence  
 227 be pre-calculated using DFT and stored.

228 **3.2. Data augmented statistical model in the Fourier domain.** The study of estima-  
 229 tors for the model (10-12) revealed as a major practical limitation the difficulty of designing  
 230 conjugate priors for the parameter vector  $\mathbf{c}_2$  since it is encoded implicitly in  $\Sigma_{j, \mathbf{c}_2}^{-1}$ , and its con-  
 231 ditional distribution is thus not standard. Sampling the posterior distribution with a Markov  
 232 chain Monte Carlo (MCMC) method was then achieved using accept/reject procedures, such  
 233 as Metropolis-Hastings (MH) moves. In view of a model expansion to multiple images (and,  
 234 hence, high-dimensional parameter vectors), such a procedure becomes quickly computation-  
 235 ally impracticable. Instead, we propose an alternative model that leads to a more efficient  
 236 algorithm (cf., [15] for a preliminary study) by interpreting (11) as a statistical model for  
 237 the Fourier coefficients  $\mathbf{y}$ . Then a suitable reparametrization is introduced that enables us to  
 238 formulate a data augmented model in which conjugate priors for  $\mathbf{c}_2$  are available.

239 **3.2.1. Fourier domain model.** To see how (11) leads to a statistical model for  $\mathbf{y}$ , we first  
 240 develop the expression using the following equivalences. First, because the log-leaders  $\{\ell(j, \mathbf{k})\}$   
 241 are real-valued, their Fourier transform  $y_j$  has the central symmetry property  $y_j(\boldsymbol{\omega}_{\mathbf{m}}) =$   
 242  $y_j^*(-\boldsymbol{\omega}_{\mathbf{m}})$ . Moreover, the parametric spectral density  $\phi_j(\boldsymbol{\omega}; \mathbf{c}_2)$  has the same property. Due  
 243 to this symmetry, only one half of the frequency plane  $J_j$  needs to be considered in the sum  
 244 in (11), which we denote by  $\underline{J}_j$ . It can for instance contain the positive frequency half-plane,  
 245 i.e.,  $\underline{J}_j \triangleq J_j \cap \{\{(i_1, i_2) \in \mathbb{Z}^2 | i_1 \geq 0\} \setminus \{(i_1, i_2) | i_1 = 0, i_2 < 0\}\}$ . Second, it is straightforward to  
 246 rewrite the first term in (11) as the inverse of the determinant of a diagonal matrix with entries  
 247  $\phi_j(\boldsymbol{\omega}_{\mathbf{m}}; \mathbf{c}_2)$ . Third, we write the sum in the second term in (11) as a matrix-vector product  
 248 by introducing the operator  $\mathcal{F}_{\underline{J}_j}(\cdot)$  computes and vectorizes the DFT coefficients contained in  
 249 the half-plane  $\underline{J}_j$ . With these ingredients, (11) can be developed into

$$250 \quad (13) \quad p^\dagger(\ell_j | \mathbf{c}_2) = \det(\boldsymbol{\Gamma}_{j, \mathbf{c}_2})^{-1} \exp\left(-\mathbf{y}_j^H \boldsymbol{\Gamma}_{j, \mathbf{c}_2}^{-1} \mathbf{y}_j\right), \quad \mathbf{y}_j \triangleq \mathcal{F}_{\underline{J}_j}(\ell_j)$$

251 where  $^H$  is the conjugate transpose operator and  $\boldsymbol{\Gamma}_{j, \mathbf{c}_2}$  is the diagonal matrix defined by

$$252 \quad (14) \quad \boldsymbol{\Gamma}_{j, \mathbf{c}_2} \triangleq c_2 \mathbf{F}_j + c_2^0 \mathbf{G}_j$$

$$253 \quad \mathbf{F}_j \triangleq \text{diag}(\mathbf{f}_j) \quad \text{with} \quad \mathbf{f}_j \triangleq (h_j^{(1)}(\boldsymbol{\omega}_{\mathbf{m}}))_{\mathbf{m} \in \underline{J}_j}$$

$$254 \quad \mathbf{G}_j \triangleq \text{diag}(\mathbf{g}_j) \quad \text{with} \quad \mathbf{g}_j \triangleq (h_j^{(2)}(\boldsymbol{\omega}_{\mathbf{m}}))_{\mathbf{m} \in \underline{J}_j}.$$

256 By inspection of (13), modeling  $\ell_j$  using  $p^\dagger(\ell_j | \mathbf{c}_2)$  is equivalent to modeling  $\mathbf{y}_j = \mathcal{F}_{\underline{J}_j}(\ell_j)$   
 257 by a random vector with a non-degenerate centered circular-symmetric complex Gaussian  
 258 distribution  $\mathcal{CN}(\mathbf{0}, \boldsymbol{\Gamma}_{j, \mathbf{c}_2})$  [22, 43], provided the matrix  $\boldsymbol{\Gamma}_{j, \mathbf{c}_2}$  is positive definite (PD). We  
 259 therefore propose to consider the Fourier coefficients  $\mathbf{y}_j = \mathcal{F}_{\underline{J}_j}(\ell_j)$ ,  $j = j_1, \dots, j_2$ , as the  
 260 observed data with likelihood

$$261 \quad (15) \quad p(\mathbf{y}_j | \mathbf{c}_2) = |\boldsymbol{\Gamma}_{j, \mathbf{c}_2}|^{-1} \exp\left(-\mathbf{y}_j^H \boldsymbol{\Gamma}_{j, \mathbf{c}_2}^{-1} \mathbf{y}_j\right)$$

262 instead of the log-leaders  $\ell_j$  with likelihood (9).

263 Assuming independence between scales  $j$  as in the direct model (10), the likelihood for  
 264 the vector  $\mathbf{y} \triangleq [\mathbf{y}_{j_1}^T, \dots, \mathbf{y}_{j_2}^T]^T$  replacing (10) is given by

$$265 \quad (16) \quad p(\mathbf{y} | \mathbf{c}_2) \triangleq \prod_{j=j_1}^{j_2} p(\mathbf{y}_j | \mathbf{c}_2) \propto |\boldsymbol{\Gamma}_{\mathbf{c}_2}|^{-1} \exp\left(-\mathbf{y}^H \boldsymbol{\Gamma}_{\mathbf{c}_2}^{-1} \mathbf{y}\right)$$

266 where  $\boldsymbol{\Gamma}_{\mathbf{c}_2}$  is the  $N_Y \times N_Y$  diagonal covariance matrix,  $N_Y \triangleq \text{card}(\mathbf{y})$ , defined as

$$267 \quad (17) \quad \boldsymbol{\Gamma}_{\mathbf{c}_2} \triangleq c_2 \mathbf{F} + c_2^0 \mathbf{G}$$

$$268 \quad \mathbf{F} \triangleq \text{diag}(\mathbf{f}) \quad \text{with} \quad \mathbf{f} \triangleq [\mathbf{f}_{j_1}^T, \dots, \mathbf{f}_{j_2}^T]^T$$

$$269 \quad \mathbf{G} \triangleq \text{diag}(\mathbf{g}) \quad \text{with} \quad \mathbf{g} \triangleq [\mathbf{g}_{j_1}^T, \dots, \mathbf{g}_{j_2}^T]^T.$$

271 In contrast to (10), the admissible set for  $\mathbf{c}_2 = (c_2, c_2^0)$  that ensures that the matrix  $\boldsymbol{\Gamma}_{\mathbf{c}_2}$  is PD  
 272 (and hence (16) is a valid likelihood) can now be expressed explicitly as

$$273 \quad (18) \quad \mathcal{A} = \{\mathbf{c}_2 \in \mathbb{R}_{<0} \times \mathbb{R}_{<0} | c_2 \mathbf{f}(k) + c_2^0 \mathbf{g}(k) > 0, k = 1, \dots, N_Y\}.$$



274 **3.2.2. Reparametrization.** The likelihood (16) and the constraints (18) are not separable  
 275 in  $c_2$  and  $c_2^0$ , which prevents the design of independent conjugate priors for  $c_2$  and  $c_2^0$ . To  
 276 circumvent this difficulty, we propose a suitable reparametrization that enables an augmented  
 277 model, associated with a separable extended likelihood leading to  $\mathcal{IG}$  conjugate priors for the  
 278 parameters of interest. Note that, to this end, the covariance matrix  $\mathbf{\Gamma}_{c_2}$  must be decomposed  
 279 as the sum of two PD diagonal matrices, which is not the case in (17) since  $c_2\mathbf{F}$  is not PD for  
 280  $c_2 < 0$  (because there always exists an integer  $k$  such that  $\mathbf{f}(k) > 0$ ). Note that  $c_2^0\mathbf{G}$  in (17) is  
 281 in practice always PD, for  $c_2^0 > 0$ , since it can be checked that  $g(k) > 0, \forall k$  for any reasonable  
 282 image size. We thus propose to use a reparametrization defined by the mapping

$$283 \quad (19) \quad \psi : \mathbf{c}_2 \mapsto \tilde{\mathbf{c}}_2 = (\tilde{c}_{21}, \tilde{c}_{22}) \triangleq (-c_2, c_2^0/\gamma + c_2),$$

284 where  $\gamma = \sup_k \mathbf{f}(k)/\mathbf{g}(k)$ . It is easy to show that  $\psi$  is a one-to-one transformation from  $\mathcal{A}$   
 285 to  $\mathbb{R}_{>0}^2$  and hence maps the constraints (18) into independent positivity constraints,  $\tilde{c}_{2i} \in$   
 286  $\mathbb{R}_{>0}$ ,  $i = 1, 2$ . Moreover, (16) expressed with  $\tilde{\mathbf{c}}_2$  reads

$$287 \quad (20) \quad p(\mathbf{y}|\tilde{\mathbf{c}}_2) \propto |\mathbf{\Gamma}_{\tilde{\mathbf{c}}_2}|^{-1} \exp\left(-\mathbf{y}^H \mathbf{\Gamma}_{\tilde{\mathbf{c}}_2}^{-1} \mathbf{y}\right)$$

$$288 \quad (21) \quad \mathbf{\Gamma}_{\tilde{\mathbf{c}}_2} = \tilde{c}_{21}\tilde{\mathbf{F}} + \tilde{c}_{22}\tilde{\mathbf{G}}, \quad \tilde{\mathbf{F}} = -\mathbf{F} + \mathbf{G}\gamma, \quad \tilde{\mathbf{G}} = \mathbf{G}\gamma$$

289 where, by construction, the two diagonal matrices  $\tilde{c}_{21}\tilde{\mathbf{F}}$  and  $\tilde{c}_{22}\tilde{\mathbf{G}}$  are now PD for  $\tilde{\mathbf{c}}_2 \in \mathbb{R}_{>0}^2$ .

290 **3.2.3. Data augmentation.** We can now introduce an  $N_Y \times 1$  vector of latent variables  
 291  $\boldsymbol{\mu}$  that enables the likelihood (20) to be augmented using the following model

$$292 \quad (22) \quad \mathbf{y}|\boldsymbol{\mu}, \tilde{c}_{22} \sim \mathcal{CN}(\boldsymbol{\mu}, \tilde{c}_{22}\tilde{\mathbf{G}}), \quad \boldsymbol{\mu}|\tilde{c}_{21} \sim \mathcal{CN}(0, \tilde{c}_{21}\tilde{\mathbf{F}})$$

294 which is associated with the extended likelihood [20, 52]

$$295 \quad (23) \quad p(\mathbf{y}, \boldsymbol{\mu}|\tilde{\mathbf{c}}_2) \propto \tilde{c}_{22}^{-N_Y} \exp\left(-\frac{1}{\tilde{c}_{22}}(\mathbf{y} - \boldsymbol{\mu})^H \tilde{\mathbf{G}}^{-1}(\mathbf{y} - \boldsymbol{\mu})\right) \times \tilde{c}_{21}^{-N_Y} \exp\left(-\frac{1}{\tilde{c}_{21}}\boldsymbol{\mu}^H \tilde{\mathbf{F}}^{-1}\boldsymbol{\mu}\right).$$

296 It can easily be verified that the likelihood (20) is recovered by marginalization of (23) with  
 297 respect to the latent variables  $\boldsymbol{\mu}$ . Moreover, the extended likelihood (23) and the associated  
 298 constraints are both separable in  $(\tilde{c}_{21}, \tilde{c}_{22})$ .

299 **3.2.4. Prior and posterior distribution.** When  $\mathcal{IG}(\alpha_{0,i}, \beta_{0,i})$  distributions  $p(\tilde{c}_{2i})$  are used  
 300 as priors for  $\tilde{c}_{2i} \in \mathbb{R}_{>0}$ ,  $i = 1, 2$ , in (23), simple calculations show that the posterior distribu-  
 301 tion

$$302 \quad (24) \quad p(\tilde{\mathbf{c}}_2, \boldsymbol{\mu}|\mathbf{y}) \propto p(\mathbf{y}|\tilde{c}_{22}, \boldsymbol{\mu})p(\boldsymbol{\mu}|\tilde{c}_{21})p(\tilde{c}_{22})p(\tilde{c}_{21})$$

303 presents standard conditional distributions (detailed in (32a-32b) below) for the transformed  
 304 multifractal parameters  $\tilde{c}_{2i}$ . A consequence of this property is that the computational cost of  
 305 the sampler, which will be proposed to generate vectors distributed according to (24), will be  
 306 significantly reduced.

307 **4. Bayesian model for multivariate analysis.** We are now ready to specify a Bayesian  
 308 model addressing the estimation of  $c_2$  for multivariate images by using the above statistical  
 309 model and incorporating suitable joint priors.

310 **4.1. Problem formulation.**

**4.1.1. Multivariate image scenario.** We consider a (temporal, or spectral) sequence of images

$$\{\mathbf{X}_t\}, \text{ where } t \in \Omega^{(2)} \triangleq \{1, \dots, N_t\}$$

and divide each single image  $\mathbf{X}_t$  into (non-overlapping) patches as illustrated in Fig. 1 (left)

$$\mathbf{X}_{(\mathbf{x},t)}, \mathbf{x} = (x_1, x_2) \in \Omega^{(1)} \triangleq \{1, \dots, N_{x_1}\} \times \{1, \dots, N_{x_2}\}.$$

311 For notational convenience, we write  $\mathbf{s} = (\mathbf{x}, t) \in \Omega^{(1)} \times \Omega^{(2)}$ . We investigate the situation  
 312 where the (sequential or spatial) evolution of the multifractal properties between the elements  
 313  $\mathbf{X}_\mathbf{s}$  is assumed to be *smooth*. The decomposition thus enables the assessment of the temporal  
 314 / spectral evolution of the *spatially localized* (patch-wise) multifractal properties of the image.  
 315 The distinction between the spatial and the temporal/spectral component in the decomposi-  
 316 tion is meaningful because  $\mathbf{x}$  and  $t$  have different physical roles (since we deal with a sequence  
 317 of images and not an isotropic 3D data cube). This formulation is also valid for sequences of  
 318 images with spatial organization, rather than patches. Models for other multivariate image  
 319 scenarios can be obtained in a straightforward manner from the developments detailed in the  
 320 following sections. As an example, a model for non-overlapping patches of a single image was  
 321 sketched in our preliminary work [16].

322 **4.1.2. Likelihood.** For each element  $\mathbf{X}_\mathbf{s}$ , we consider the extended model (23) and we  
 323 gather the Fourier coefficients of the log-leaders  $\mathbf{y}_\mathbf{s}$  and the latent variables  $\boldsymbol{\mu}_\mathbf{s}$  for all elements  
 324  $\mathbf{s}$  in matrices  $\mathbf{Y}$  and  $\mathbf{M}$ , respectively. Moreover, let  $\tilde{\mathbf{C}}_2 = (\tilde{\mathbf{C}}_{21}, \tilde{\mathbf{C}}_{22})$  where  $\tilde{\mathbf{C}}_{2i}$  gathers the  
 325 parameters  $\tilde{c}_{2i,\mathbf{s}}$  for all  $\mathbf{s}$ . By assuming *a priori* independence between the elements  $\mathbf{X}_\mathbf{s}$ , the  
 326 joint likelihood can be generically written as

(25)

$$327 \ p(\mathbf{Y}, \mathbf{M} | \tilde{\mathbf{C}}_2) \propto \prod_{\mathbf{s}} \tilde{c}_{21,\mathbf{s}}^{-N_Y} \exp\left(-\frac{1}{\tilde{c}_{21,\mathbf{s}}} \boldsymbol{\mu}_\mathbf{s}^H \tilde{\mathbf{F}}^{-1} \boldsymbol{\mu}_\mathbf{s}\right) \tilde{c}_{22,\mathbf{s}}^{-N_Y} \exp\left(-\frac{1}{\tilde{c}_{22,\mathbf{s}}} (\mathbf{y}_\mathbf{s} - \boldsymbol{\mu}_\mathbf{s})^H \tilde{\mathbf{G}}^{-1} (\mathbf{y}_\mathbf{s} - \boldsymbol{\mu}_\mathbf{s})\right).$$

328 **4.2. Gamma Markov Random Field prior.** Inverse-gamma distributions  $\mathcal{IG}(\alpha_{i,\mathbf{s}}, \beta_{i,\mathbf{s}})$  are  
 329 conjugate priors for the parameters  $\tilde{c}_{2i,\mathbf{s}}$ . A careful design of  $(\alpha_{i,\mathbf{s}}, \beta_{i,\mathbf{s}})$ , rather than setting  
 330 them a priori to constant values, can enforce the parameters of interest  $\tilde{\mathbf{C}}_{2i}$  to vary slowly  
 331 in some privileged directions. To do so, we propose here to specify  $(\alpha_{i,\mathbf{s}}, \beta_{i,\mathbf{s}})$  such that the  
 332 resulting prior for  $\tilde{\mathbf{C}}_{2i}$  is a hidden gamma Markov random field (GaMRF) [19]. The strategy  
 333 for this prior relies on the use of a set of positive auxiliary variables  $\mathbf{Z}_i$  to induce positive  
 334 dependence between neighboring elements of  $\tilde{\mathbf{C}}_{2i}$  [19]. In what follows, we handle the spatial  
 335 and temporal/spectral components with separate variables  $\mathbf{Z}_i^{(1)}$  and  $\mathbf{Z}_i^{(2)}$ , respectively, and  
 336 denote  $\mathbf{Z}_i = (\mathbf{Z}_i^{(1)}, \mathbf{Z}_i^{(2)})$ . The distribution of the joint prior  $(\tilde{\mathbf{C}}_{2i}, \mathbf{Z}_i)$  is associated with  
 337 conditionals of the form

$$338 \ (26a) \quad \tilde{c}_{2i,\mathbf{s}} | \mathbf{Z}_i, \mathbf{a}_i \sim \mathcal{IG}(\alpha_{i,\mathbf{s}}(\mathbf{a}_i), \beta_{i,\mathbf{s}}(\mathbf{Z}_i, \mathbf{a}_i))$$

$$339 \ (26b) \quad z_{i,\mathbf{s}}^{(m)} | \tilde{\mathbf{C}}_{2i}, \mathbf{a}_i \sim \mathcal{G}(\bar{\alpha}_{i,\mathbf{s}}^{(m)}(\mathbf{a}_i), \bar{\beta}_{i,\mathbf{s}}^{(m)}(\tilde{\mathbf{C}}_{2i}, \mathbf{a}_i))$$

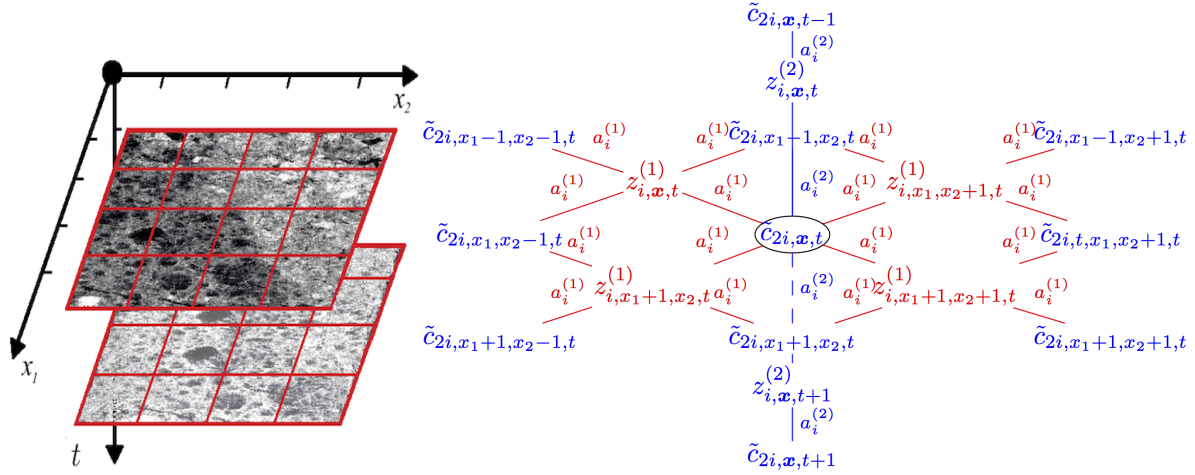


Figure 1: Illustration of multivariate image scenario (left). Spatial (red) and spectral (blue) components of the proposed bipartite conditional independence graphs between  $\tilde{\mathbf{C}}_{2i}$  and  $\mathbf{Z}_i$  (right).

341 where  $\mathcal{G}(\cdot, \cdot)$  stands for the gamma distribution and  $\mathbf{a}_i \triangleq [a_i^{(1)}, a_i^{(2)}]$  is a regularization vector  
 342 where  $a_i^{(1)}$  and  $a_i^{(2)}$  adjust the amount of spatial and temporal/spectral smoothness, re-  
 343 spectively. The parameters  $\alpha_{i,s}, \beta_{i,s}, \bar{\alpha}_{i,s}^{(m)}$  and  $\bar{\beta}_{i,s}^{(m)}$  of the  $\mathcal{IG}$  and  $\mathcal{G}$  distributions in (26)  
 344 are determined by the definition of a bipartite conditional independence graph between  $\tilde{\mathbf{C}}_{2i}$   
 345 and  $\mathbf{Z}_i^{(m)}$ . The design of the vertices and edges of the graph for the decomposition into a  
 346 spatio-temporal/spectral collection  $\{\mathbf{X}_{\mathbf{x}, t}\}_{\mathbf{x}, t \in \Omega^{(1)} \times \Omega^{(2)}}$  proposed here is sketched in Fig. 1:  
 347 Correlation between the parameters of neighboring patches is induced by two sets of aux-  
 348 iliary variables  $\mathbf{Z}_i^{(1)} = \{z_{i, \mathbf{x}, t}^{(1)}\}_{\mathbf{x}, t \in \Omega^{(1)} \times \Omega^{(2)}}$  and  $\mathbf{Z}_i^{(2)} = \{z_{i, \mathbf{x}, t}^{(2)}\}_{\mathbf{x}, t \in \Omega^{(1)} \times \Omega^{(2)}}$ ,  $z_{i, \mathbf{x}, t}^{(1)} \in \mathbb{R}_{>0}$  and  
 349  $z_{i, \mathbf{x}, t}^{(2)} \in \mathbb{R}_{>0}$ , using a graph that connects each  $\tilde{c}_{2i, \mathbf{x}, t}$  to its four natural spatial neighbors in  
 350  $\mathbf{Z}_i^{(1)}$  and to its two natural temporal neighbors in  $\mathbf{Z}_i^{(2)}$ , and vice-versa. Notably, by doing  
 351 so,  $\tilde{c}_{2i, \mathbf{x}, t}$  and  $\tilde{c}_{2i, x_1, x_2-1, t}$  are connected via  $z_{i, \mathbf{x}, t}^{(1)}$  and  $z_{i, x_1+1, x_2, t}^{(1)}$  over edges with weight  $a_i^{(1)}$ ,  
 352 and  $\tilde{c}_{2i, \mathbf{x}, t}$  are connected to  $\tilde{c}_{2i, \mathbf{x}, t-1}$  via  $z_{i, \mathbf{x}, t}^{(2)}$  over edges with weight  $a_i^{(2)}$ . The density of the  
 353 resulting GaMRF prior for  $(\tilde{\mathbf{C}}_{2i}, \mathbf{Z}_i)$  is then given by [19]

$$\begin{aligned}
 354 \quad p(\tilde{\mathbf{C}}_{2i}, \mathbf{Z}_i | \mathbf{a}_i) &= \frac{1}{K(\mathbf{a}_i)} \prod_{\mathbf{x} \in \Omega^{(1)}} \prod_{t \in \Omega^{(2)}} \Phi_{\mathcal{I}}(\tilde{c}_{2i, \mathbf{x}, t}; 4a_i^{(1)} + 2a_i^{(2)}) \\
 355 \quad &\times \prod_{\mathbf{x} \in \Omega^{(1)}} \prod_{t \in \Omega^{(2)}} \Phi_{\mathcal{G}}(z_{i, \mathbf{x}, t}^{(1)}; 4a_i^{(1)}) \times \prod_{\mathbf{x} \in \Omega^{(1)}} \prod_{t \in \Omega^{(2)}} \Phi_{\mathcal{G}}(z_{i, \mathbf{x}, t}^{(2)}; 2a_i^{(2)}) \\
 356 \quad (27) \quad &\times \prod_{\mathbf{x} \in \Omega^{(1)}} \prod_{t \in \Omega^{(2)}} \Phi\left(a_i^{(2)} \sum_{t' \in \mathcal{V}_{\tilde{\mathbf{c}}_2}^{(1)}(t)} z_{i, \mathbf{x}, t'}^{(2)} + a_i^{(1)} \sum_{\mathbf{x}' \in \mathcal{V}_{\tilde{\mathbf{c}}_2}^{(2)}(\mathbf{x})} z_{i, \mathbf{x}', t}^{(1)}, \tilde{c}_{2i, \mathbf{x}, t}\right) \\
 357 \quad &
 \end{aligned}$$

358 where we have introduced  $\Phi_{\mathcal{I}}(\xi; \alpha) \triangleq \exp(-(\alpha + 1) \log \xi)$ ,  $\Phi_{\mathcal{G}}(\xi; \alpha) \triangleq \exp((\alpha - 1) \log \xi)$  and  
 359  $\Phi(\xi, \delta) \triangleq \exp(-\xi/\delta)$  for convenience of notation and where  $K(\mathbf{a}_i)$  is a normalizing constant.  
 360 The sums in (27) are taken over the neighborhoods

$$\begin{aligned}
 361 \quad \mathcal{V}_{\tilde{\mathbf{c}}_2}^{(1)}(\mathbf{x}) &= \{(x_1, x_2), (x_1 + 1, x_2), (x_1, x_2 + 1), (x_1 + 1, x_2 + 1)\}, \\
 362 \quad \mathcal{V}_z^{(1)}(\mathbf{x}) &= \{(x_1 - 1, x_2 - 1), (x_1, x_2 - 1), (x_1 - 1, x_2), (x_1, x_2)\}, \\
 363 \quad \mathcal{V}_{\tilde{\mathbf{c}}_2}^{(2)}(t) &= \{t, t + 1\}, \quad \mathcal{V}_z^{(2)}(t) = \{t - 1, t\},
 \end{aligned}$$

365 which are the indices of variables that define the neighborhoods of  $\tilde{\mathbf{c}}_{2i, \mathbf{x}, t}$  and  $z_{i, \mathbf{x}, t}^{(1)}$  and  $z_{i, \mathbf{x}, t}^{(2)}$ ,  
 366 respectively. The parameters of the associated conditionals (26a) and (26b) are

$$367 \quad (28a) \quad \alpha_{i, \mathbf{x}, t} = 4a_i^{(1)} + 2a_i^{(2)}, \quad \beta_{i, \mathbf{x}, t} = a_i^{(1)} \sum_{\mathbf{x}' \in \mathcal{V}_{\tilde{\mathbf{c}}_2}^{(1)}(\mathbf{x})} z_{i, \mathbf{x}', t}^{(1)} + a_i^{(2)} \sum_{t' \in \mathcal{V}_{\tilde{\mathbf{c}}_2}^{(2)}(t)} z_{i, \mathbf{x}, t'}^{(2)}$$

$$368 \quad (28b) \quad \bar{\alpha}_{i, \mathbf{x}, t}^{(1)} = 4a_i^{(1)}, \quad \bar{\beta}_{i, \mathbf{x}, t}^{(1)} = \left( a_i^{(1)} \sum_{\mathbf{x}' \in \mathcal{V}_z^{(1)}(\mathbf{x})} \tilde{\mathbf{c}}_{2i, \mathbf{x}', t}^{-1} \right)^{-1}$$

$$369 \quad (28c) \quad \bar{\alpha}_{i, \mathbf{x}, t}^{(2)} = 2a_i^{(2)}, \quad \bar{\beta}_{i, \mathbf{x}, t}^{(2)} = \left( a_i^{(2)} \sum_{t' \in \mathcal{V}_z^{(2)}(t)} \tilde{\mathbf{c}}_{2i, \mathbf{x}, t'}^{-1} \right)^{-1}.$$

372 **4.3. Joint posterior distribution.** Using Bayes' theorem and assuming prior indepen-  
 373 dence between  $(\tilde{\mathbf{C}}_{21}, \mathbf{Z}_1)$  and  $(\tilde{\mathbf{C}}_{22}, \mathbf{M}, \mathbf{Z}_2)$ , the joint posterior distribution associated with  
 374 the proposed Bayesian model is

$$375 \quad (29) \quad p(\tilde{\mathbf{C}}_2, \mathbf{Z}, \mathbf{M} | \mathbf{Y}, \{\mathbf{a}_i\}) \propto p(\mathbf{Y} | \tilde{\mathbf{C}}_{22}, \mathbf{M}) p(\mathbf{M} | \tilde{\mathbf{C}}_{21}) \times p(\tilde{\mathbf{C}}_{21}, \mathbf{Z}_1 | \mathbf{a}_1) p(\tilde{\mathbf{C}}_{22}, \mathbf{Z}_2 | \mathbf{a}_2)$$

376 with  $\mathbf{Z} = (\mathbf{Z}_1, \mathbf{Z}_2)$  and where the regularization hyperparameters  $\mathbf{a}_i$  are fixed a priori (the  
 377 estimation of  $\mathbf{a}_i$ , given that the normalizing constant  $K(\mathbf{a}_i)$  is intractable, is not considered  
 378 here for the sake of clarity and focus, cf., e.g., [7, 25, 40, 45] for methods addressing such  
 379 situations).

## 380 5. Bayesian Inference.

381 **5.1. Bayesian estimators.** The knowledge of the unknown multifractal parameters  $\tilde{\mathbf{C}}_{2i}$   
 382 given the observed data and the prior information assigned to the different model parameters  
 383 is summarized in the posterior distribution (29). We consider here the marginal posterior  
 384 mean estimator for  $\tilde{\mathbf{C}}_{2i}$ , denoted by the superscript MMSE for minimum mean square error  
 385 estimator and defined as

$$386 \quad (30) \quad \tilde{\mathbf{C}}_{2i}^{\text{MMSE}} \triangleq \mathbb{E}[\tilde{\mathbf{C}}_{2i} | \mathbf{Y}, \mathbf{a}_i]$$

387 where the expectation is taken with respect to the marginal posterior density  $p(\tilde{\mathbf{C}}_{2i} | \mathbf{Y}, \mathbf{a}_i)$ .  
 388 The direct computation of (30) is intractable as it requires integrating the posterior (29) over  
 389 all other unknown variables. However (30) can be approximated with an arbitrary precision  
 390 by resorting to an MCMC algorithm [46]. Here we consider a Gibbs sampler drawing samples  
 391  $(\tilde{\mathbf{C}}_2^{(q)}, \mathbf{M}^{(q)}, \mathbf{Z}^q)_{q=1}^{N_{mc}}$  that are asymptotically distributed according to the targeted joint pos-  
 392 terior (29). These samples are used in turn to approximate the marginal posterior mean (30)  
 393 by  $\tilde{\mathbf{C}}_{2i}^{\text{MMSE}} \approx (N_{mc} - N_{bi})^{-1} \sum_{q=N_{bi}+1}^{N_{mc}} \tilde{\mathbf{C}}_{2i}^{(q)}$  [46], where  $N_{bi}$  is the length of the burn-in period.

394 **5.2. Gibbs sampler.** The strategy of the Gibbs sampler consists of successively generating  
 395 samples from the conditional distributions associated with the posterior. It is easy to show  
 396 that the conditional distributions associated with the posterior (29) are given by

$$397 \quad (31a) \quad \boldsymbol{\mu}_s | \mathbf{Y}, \tilde{\mathbf{C}}_2 \sim \mathcal{CN} \left( \tilde{c}_{21,s} \tilde{\mathbf{F}} \boldsymbol{\Gamma}_{\tilde{\mathbf{C}}_2,s}^{-1} \mathbf{y}_s, \left( (\tilde{c}_{21,s} \tilde{\mathbf{F}})^{-1} + (\tilde{c}_{22,s} \tilde{\mathbf{G}})^{-1} \right)^{-1} \right)$$

$$398 \quad (31b) \quad \tilde{c}_{21,s} | \mathbf{M}, \mathbf{Z}_1 \sim \mathcal{IG} \left( N_Y + \alpha_{1,s}, \|\boldsymbol{\mu}_s\|_{\tilde{\mathbf{F}}}^{-1} + \beta_{1,s} \right)$$

$$399 \quad (31c) \quad \tilde{c}_{22,s} | \mathbf{Y}, \mathbf{M}, \mathbf{Z}_2 \sim \mathcal{IG} \left( N_Y + \alpha_{2,s}, \|\mathbf{y}_s - \boldsymbol{\mu}_s\|_{\tilde{\mathbf{G}}}^{-1} + \beta_{2,s} \right)$$

$$400 \quad (31d) \quad z_{i,s}^{(m)} | \tilde{\mathbf{C}}_{2i} \sim \mathcal{G}(\bar{\alpha}_{i,s}^{(m)}, \bar{\beta}_{i,s}^{(m)})$$

402 where  $\|\mathbf{x}\|_{\mathbf{M}} \triangleq \mathbf{x}^H \mathbf{M} \mathbf{x}$ . We recall that  $\boldsymbol{\Gamma}_{\tilde{\mathbf{C}}_2,s} \triangleq \tilde{c}_{21,s} \tilde{\mathbf{F}} + \tilde{c}_{22,s} \tilde{\mathbf{G}}$  and that  $\alpha_{i,s}, \beta_{i,s}, \bar{\alpha}_{i,s}^{(m)}$  and  
 403  $\bar{\beta}_{i,s}^{(m)}$  are defined in (28). Note that all conditional distributions are standard and thus can be  
 404 sampled efficiently, without MH accept-reject steps. This property is a direct consequence of  
 405 the proposed extended model (23) (involving  $\mathcal{IG}$  conjugate priors) and enables the estimation  
 406 of large unknown parameter vectors  $\tilde{\mathbf{C}}_{2i}$ .

407 Finally, note that when each  $\tilde{c}_{2i,s}$  is modeled independently with the univariate model  
 408 (24) (i.e., the parameters  $\tilde{c}_{2i,s}$  have inverse-gamma priors  $\mathcal{IG}(\alpha_{0,i}, \beta_{0,i})$  with a priori fixed  
 409 parameters  $\alpha_{0,i}, \beta_{0,i}$  instead of the GaMRF priors of Section 4.2), the conditional distributions  
 410 are given by (31a) and

$$411 \quad (32a) \quad \tilde{c}_{21,s} | \mathbf{M} \sim \mathcal{IG} \left( N_Y + \alpha_{0,1}, \|\boldsymbol{\mu}_s\|_{\tilde{\mathbf{F}}}^{-1} + \beta_{0,1} \right)$$

$$412 \quad (32b) \quad \tilde{c}_{22,s} | \mathbf{Y}, \mathbf{M} \sim \mathcal{IG} \left( N_Y + \alpha_{0,2}, \|\mathbf{y}_s - \boldsymbol{\mu}_s\|_{\tilde{\mathbf{G}}}^{-1} + \beta_{0,2} \right)$$

414 ((31d) is discarded in this model). Moreover, it is easy to see that the model can be straight-  
 415 forwardly adapted to situations in which data components (i.e., elements of  $\mathbf{Y}$ ) are corrupted  
 416 or missing, in which case estimates for the affected parameters can be obtained by sampling  
 417 from the corresponding components of the multivariate prior.

418 **6. Numerical results for synthetic data.** In this section, we compare the proposed Bayesian  
 419 approach using joint GaMRF priors (i.e., the multivariate model leading to (31a-31d),  
 420 denoted as GaMRF) to the method using independent  $\mathcal{IG}$  priors (i.e., the novel univariate  
 421 model (24) leading to (32a-32b), denoted as IG) and to the standard linear regression based  
 422 method (using (7) and denoted as LF). The comparison is performed by running the different  
 423 methods on a large number of independent realizations of sequences of heterogeneous synthetic  
 424 multifractal images.

425 **6.1. Synthetic multifractal image sequence.** The scenario considered here is summarized  
 426 in Fig. 2(a): Each realization of the synthetic data set consists of a sequence of 50 independent  
 427 2D multifractal random walks (MRW) of size  $3200 \times 3200$ . A MRW is chosen here because its  
 428 multifractal properties mimic those of Mandelbrot's celebrated log-normal cascades [37] and  
 429 for its ease of numerical synthesis. Its multifractal spectrum is given by (6) with  $c_1 > 0.5$ ,  
 430  $c_2 < 0$  and  $c_p = 0, p \geq 3$  (cf., [47]). Each 2D MRW in the sequence, indexed by  $t$ , has two  
 431 distinct multifractal regions whose geometry has been fixed for all  $t$  and comprises a back-

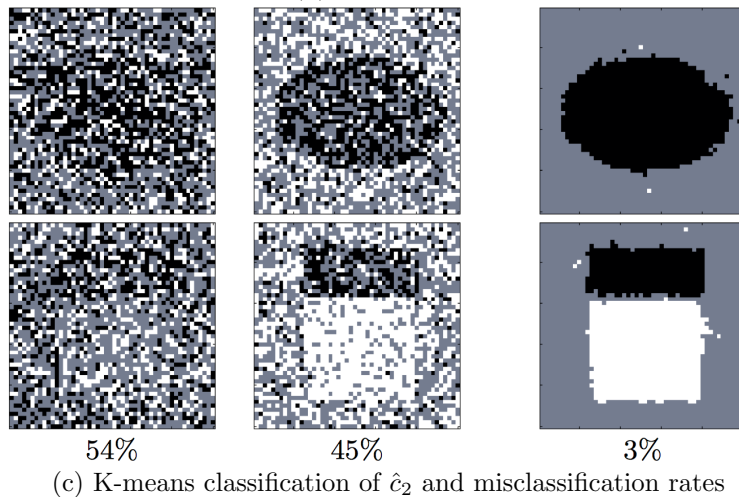
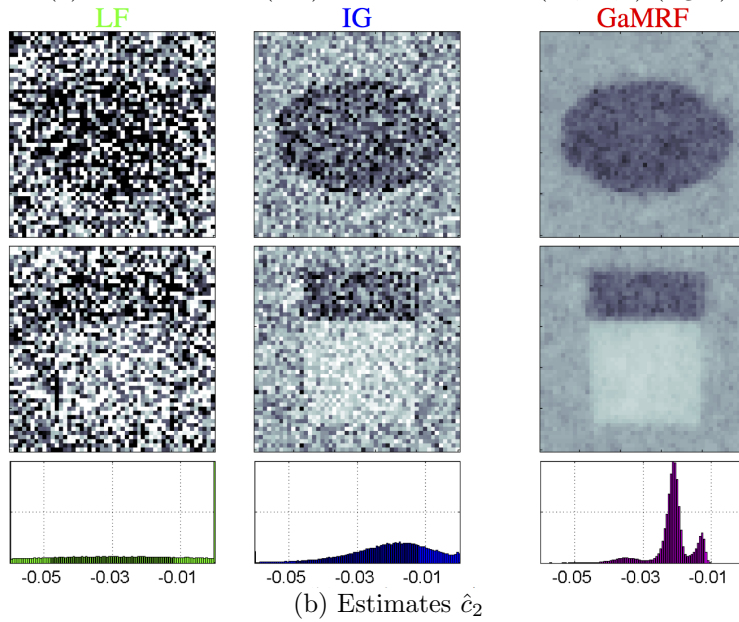
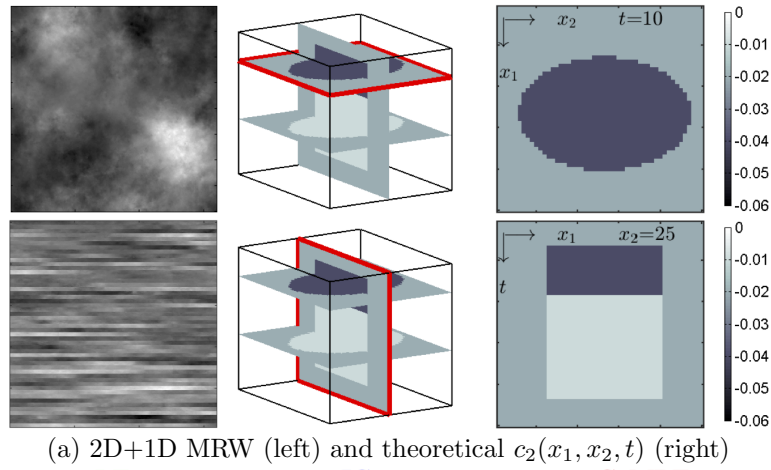


Figure 2: Estimation results for a temporal sequence of heterogeneous MRWs decomposed into  $50 \times 50 \times 50$  patches of size  $2^6 \times 2^6$ : prescribed  $c_2$  masks (a); estimates  $\hat{c}_2$  for two different slices and overall histograms (b); classification labels obtained by histogram thresholding and misclassification rates (c).

432 ground with  $c_2 = -0.02$  that includes an ellipse for which  $c_2$  evolves with  $t$  according to a piece-  
 433 wise constant profile. An example of a realization of heterogeneous 2D MRW (corresponding  
 434 to frame  $t = 30$ ) is displayed in Fig. 2(a) (top left). Note that the piece-wise constant  
 435 evolution of  $c_2$  (in space and along  $t$ ) is intentionally chosen here as a limit test case for the  
 436 robustness of the proposed approach (which assumes a smooth evolution of  $c_2$  in the data).

437 **6.2. Experimental setup.** A Daubechies' mother wavelet with  $N_\psi = 2$  vanishing moments  
 438 is used in the 2D DWT. The linear regression weights  $w_j$  in (5) are chosen proportional to  
 439  $n_j$ , cf., e.g., [54, 58]. Following [17], the frequencies  $J_j$  in (11) (and, hence,  $\underline{J}_j$  in (13))  
 440 are restricted to  $0 < \|\omega_{\mathbf{m}}\| < \pi/4$  for all Bayesian estimators. The values of the GaMRF  
 441 parameters were set to  $(a_i^{(1)}, a_i^{(2)}) = (10, 20)$  based on visual comparison of preliminary results  
 442 obtained for a range of values for  $(a_i^{(1)}, a_i^{(2)})$ . The hyperparameters of the independent  $\mathcal{IG}$   
 443 priors for IG were set to  $(\alpha_{0,i}, \beta_{0,i}) = (10^{-3}, 10^{-3})$ , which ensures that they closely resemble a  
 444 non-informative Jeffreys' prior. The estimation is performed on a decomposition of the cube  
 445 into  $N_{x_1} \times N_{x_2} \times N_t = 50 \times 50 \times 50$  patches of size  $2^6 \times 2^6$ . The estimation performance is  
 446 quantified as the average  $\mathfrak{m} \triangleq \widehat{\mathbb{E}}[\hat{c}_2]$ , the standard deviation (STD)  $s = (\widehat{\text{Var}}[\hat{c}_2])^{\frac{1}{2}}$  and the root  
 447 mean squared error (RMSE)  $\text{rms} = \sqrt{(\mathfrak{m} - c_2)^2 + s^2}$ , where  $\widehat{\mathbb{E}}$  and  $\widehat{\text{Var}}$  stand for the sample  
 448 mean and variance, respectively, evaluated over 100 independent realizations.

449 **6.3. Results.**

450 **6.3.1. Illustration for a single realization.** We first illustrate the performance of the  
 451 different estimation methods for one single realization of the above described sequence of  
 452 synthetic images. Fig. 2(b) plots estimates  $\hat{c}_2$  for frame  $t = 10$  (first row), and a slice along  $t$   
 453 for  $x_2 = 25$  (second row) together with the histograms of estimates (third row) for LF, IG and  
 454 GaMRF (left, center and right column, respectively). The corresponding theoretical values  
 455 for  $c_2$  are plotted in Fig. 2(a).

456 Clearly, LF exhibits strong spatial and temporal variability and fails to provide a smooth  
 457 evolution of the multifractality in the dataset. The Bayesian estimator IG with non-infor-  
 458 mative prior improves the estimation accuracy with respect to LF and enables the visual  
 459 identification (in time and space) of the zones with different multifractality, yet estimates ob-  
 460 tained with IG still display strong variability and their histogram does not reveal the existence  
 461 of three distinct zones of multifractality in the data. In contrast to these univariate estimators,  
 462 the proposed GaMRF estimator provides more satisfactory results with increased spatial and  
 463 temporal coherence and significantly reduced variability of the estimates. In particular, the  
 464 estimates obtained with GaMRF lead to histograms in which the three different values for  $c_2$   
 465 in the data are reflected as pronounced and well separated peaks.

466 A more quantitative analysis of these results is proposed in Fig. 2(c), which shows the  
 467 results of a classification of the estimates, obtained by histogram thresholding using the  $k$ -  
 468 means algorithm with 3 classes (the classes have been attributed in order to yield lowest  
 469 misclassification error). The misclassification rates achieved by the different algorithms are  
 470 54% for LF and 45% for IG, but only 3% for GaMRF, thus showing the ability of the proposed  
 471 procedure to perform a relevant multivariate estimation for  $c_2$ .

	LF	IG	GaMRF
$ m - c_2 $	0.0057	0.0017	0.0023
s	0.038	0.011	0.0016
rmse	0.039	0.011	0.0029

Table 1: Absolute values of bias  $|m - c_2|$ , standard deviations s and RMSE values rmse for the different estimators (results obtained for 100 independent realizations).

472 **6.3.2. Estimation performance.** Fig. 3 plots estimation performance, evaluated over 100  
473 independent realizations, as a function of  $x$  (for  $t = 10, x_2 = 25$ ) and of  $t$  (for  $x_1 = 25, x_2 = 25$ ).  
474 The overall performance for the image sequence is given in Tab. 1. First, a comparison of  
475 the average of estimates for the Bayesian estimators leads to the conclusion that, despite  
476 the departure of the scenario considered from the assumption of slow evolution for  $c_2$ , the  
477 GaMRF estimator yields average profiles close to that of IG. Only close to sharp transitions  
478 for the value of  $c_2$  does GaMRF introduce some bias due to the smoothing effect of the  
479 prior. Yet, this effect remains confined to  $\pm 3$  neighboring patches and has little impact on  
480 the overall bias reported in Tab. 1. Estimates obtained with LF are found to have the largest  
481 (by a factor of 3) bias. Second, while the Bayesian estimator IG with non-informative prior  
482 already yields a remarkable reduction of variability compared to LF (STD values are divided  
483 by 4), the proposed multivariate GaMRF estimator further and dramatically decreases STD  
484 to values that are more than one order of magnitude below those of LF. This is also reflected  
485 by the overall STD and RMSE values reported in Tab. 1, which are more than one order of  
486 magnitude better for GaMRF than for LF. Due to the bias introduced by GaMRF close to  
487 sharp transitions of the value of  $c_2$ , local RMSE values range from 25% (close to transitions) to  
488 only 4% (in homogeneous areas) of those of LF. Finally, note that these significant performance  
489 gains of GaMRF are achieved at very reasonable computational cost. As an example, the  
490 analysis of a  $1024 \times 1024 \times 50$  data cube using patches of size  $64 \times 64$  takes about 100  
491 seconds for GaMRF on a standard desktop computer <sup>2</sup>, which is only 4 times more than  
492 what the LF method requires. The cost of IG is similar to that of GaMRF. Note that the  
493 direct space-domain statistical model of Section 3.1 leads to two orders of magnitude larger  
494 computational cost (and, by construction, similar performance as IG) [17]. Overall, these  
495 results demonstrate the clear practical benefits of the proposed procedure for the multifractal  
496 analysis of multivariate images.

497 **7. Application to real-world images.** Finally we illustrate the application of the proposed  
498 joint estimator for the multifractality parameter to two real-world multivariate remote sensing  
499 images of different natures: a hyperspectral (HS) image, and a multi-temporal (MT) image.

500 **7.1. Application to a hyperspectral image.** The HS image under study corresponds to  
501 a forested area near a city and was acquired by the Hypsrex hyperspectral scanner during the  
502 Madonna project [51]. It contains  $960 \times 1952$  pixels with a spatial resolution of 0.5 meters and  
503 160 spectral bands ranging from the visible to near infrared. In our numerical experiment,

<sup>2</sup>Using Matlab, a 3.40 Ghz Intel Core i7 processor and 8GB RAM



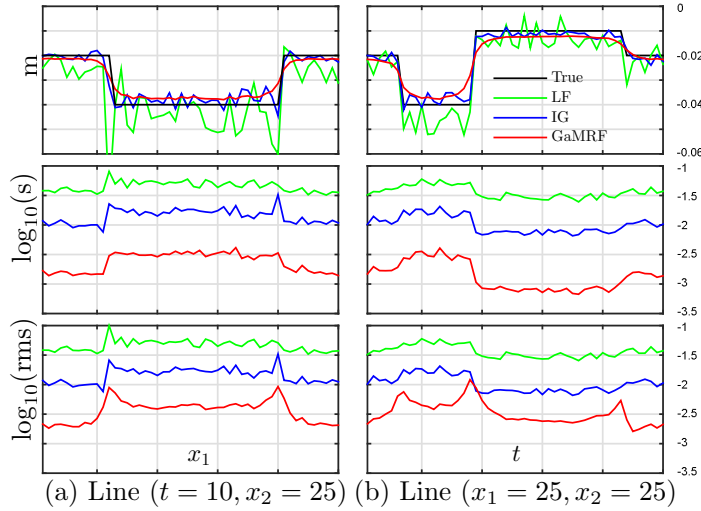


Figure 3: Estimation performance for heterogeneous 2D MRWs: mean (first row), standard deviation (second row) and root-mean square error (third row) in (a) spatial direction  $x_1$  ( $t = 10, x_2 = 25$ ) and (b) temporal direction  $t$  ( $x_1 = 25, x_2 = 25$ ).

504 the 80 last bands are analyzed. Each band is decomposed into  $29 \times 60$  patches of size  $64 \times 64$   
 505 pixels, with 50% overlap, resulting in a decomposition into  $29 \times 60 \times 80$  patches indexed by  
 506  $(x_1, x_2, k_\lambda)$ , where  $k_\lambda$  stands for the spectral dimension. Overlapping patches are chosen here  
 507 in order to increase the spatial resolution and to illustrate the robustness of the model (even  
 508 if the independence assumption between patches is clearly violated when they overlap).

509 The subplots in Fig. 4 report the estimates for the multifractality parameter  $c_2$  provided  
 510 by LF, IG and GaMRF for two representative spectral bands (c) (the bands 87 and 114, which  
 511 are plotted in (b)) as well as for a slice along the spectral dimension (d) (the corresponding  
 512  $64 \times 1962 \times 80$  portion of the HS cube is indicated by a red frame in (a)). A visual inspection  
 513 of the results for the bands 87 and 114 reveals that the strong spatial variability of the  
 514 estimates obtained with LF prevents the identification of distinct regions in the image (with  
 515 the exception perhaps of the city in the left bottom corner which yields clusters of strongly  
 516 negative  $c_2$ ). The estimator IG yields better spatial coherence and clearly improves over the  
 517 estimates obtained with LF (see [17] for a similar experiment for one single spectral band  
 518 using the model (10-11), leading to the same conclusions). Yet, the variability within visually  
 519 homogeneous zones of the dataset (e.g., the forested region) is still important. In comparison  
 520 with IG, and a fortiori with LF, the proposed GaMRF method further and dramatically  
 521 reduces the variability within presumably homogeneously multifractal zones, inducing strong  
 522 spatial coherence, which reinforces the contrast between regions of different multifractalities  
 523 and visually sharpens their borders. As a result, these estimates can potentially reveal hidden  
 524 underlying structures in the data set. Despite the absence of a ground truth for this data set we  
 525 can, for instance, observe that the forested area in the right half of the image is homogeneous  
 526 (with  $c_2 \sim -0.05$ ) in the spectral band  $k_\lambda = 114$ , while it is composed of a background (where  
 527  $c_2 \sim -0.05$ ) and scattered clusters (where  $c_2 \sim -0.1$ ) in the spectral band  $k_\lambda = 87$ , which

528 could arguably indicate a physical change at this location (e.g., a lower tree density). Finally,  
 529 the spectral evolution of  $c_2$ , plotted in Fig. 4(d), reveals the strong spectral redundancy that  
 530 is generally observed for HS data, cf., e.g., [12]. Nevertheless, the proposed GaMRF estimator  
 531 permits a reduction in the variance of estimates along the spectral dimension and yields a  
 532 visually less noisy evolution of  $c_2$  across the bands of the image, while maintaining its main  
 533 features.

534 **7.2. Application to a multi-temporal image.** We further perform the multifractal anal-  
 535 ysis of an MT image with 11 time frames. Each frame consists of a  $900 \times 900$  pixel image  
 536 with a spatial resolution of about 0.2 meters, captured in 140 spectral band recorded from the  
 537 visible to near infrared (415 to 990 nm; only one single band is analyzed here). The images  
 538 were acquired over the same rural scene at Porton Down in the U.K. over a 2-day period  
 539 (data courtesy of DSTL). The recorded scene comprises several roads and tracks between  
 540 open fields, a few trees, as well as two man-made “targets” (visible as distinct white crosses).  
 541 Two frames for  $t = 2$  and  $t = 8$  are plotted in Fig. 5 (a), showing that the image is subject  
 542 to considerable changes in (partial) illumination across time. As in the previous section, each  
 543 frame is decomposed in patches of size  $64 \times 64$  pixels, with 50% overlap, resulting in a decom-  
 544 position into  $27 \times 27 \times 11$  patches, indexed by  $(x_1, x_2, t)$ . Visual inspection of the estimates  
 545 for  $c_2$  provided by LF, IG and GaMRF for the frames  $t = 2$  and  $t = 8$ , plotted in Fig. 5(b),  
 546 first leads to conclusions similar to those obtained in Section 7.1: the strong variability of LF  
 547 prevents from identifying any of the spatial image features; the IG estimates yield acceptable  
 548 spatial coherence; the GaMRF estimator leads to the visually most satisfactory results and  
 549 yields much less speckled estimates for the image regions that can be considered homogeneous  
 550 (i.e., the fields) as well as sharp contrast for the artificial structures (roads, targets). In addi-  
 551 tion, it can be observed that the proposed GaMRF estimator permits better tracking of image  
 552 features across time. This is, for instance, the case for the road indicated by red arrows in Fig.  
 553 5(b), which is at best partially visible in frame  $t = 8$  for IG (and not at all for LF), probably  
 554 due to insufficient illumination for this frame, but can be clearly and easily identified for the  
 555 estimates obtained with GaMRF. The evolution of  $c_2$  across time is further investigated in  
 556 Fig. 5(c) and (d), where a longitudinal and a lateral slice of the multi-temporal estimates are  
 557 plotted. Visual inspection leads us to conclude that GaMRF yields very consistent estimates  
 558 across time. Since the multifractal parameters are invariant to (spatially smooth) changes in  
 559 illumination, this is to be expected for a scene in which only the illumination varies but the  
 560 scene itself does not vary. In contrast, IG and even more so LF display significant temporal  
 561 noise. As a result, the proposed GaMRF estimator enables us to coherently render particular  
 562 image features across time that are harder to identify for IG and LF, e.g., for the zone of strong  
 563 multifractality ( $c_2 \simeq -0.1$ ) in the vicinity of the trees in the upper left corner of the image  
 564 frames, corresponding to the vertical strip of estimates for  $c_2$ , indicated by orange arrows in  
 565 Fig. 5(d).

566 **8. Discussion and Conclusion.** The present paper introduced a novel Bayesian procedure  
 567 for the joint estimation of the multifractality parameter for (patches of) multivariate images.  
 568 It builds on two original key contributions. First, it is based on an extended likelihood for  
 569 the Fourier coefficients of log-leaders of a single image, separable in the parameters of inter-  
 570 est ( $c_2, c_2^0$ ). Second, it models the collection of unknown (multifractal) parameters  $c_2$  of a

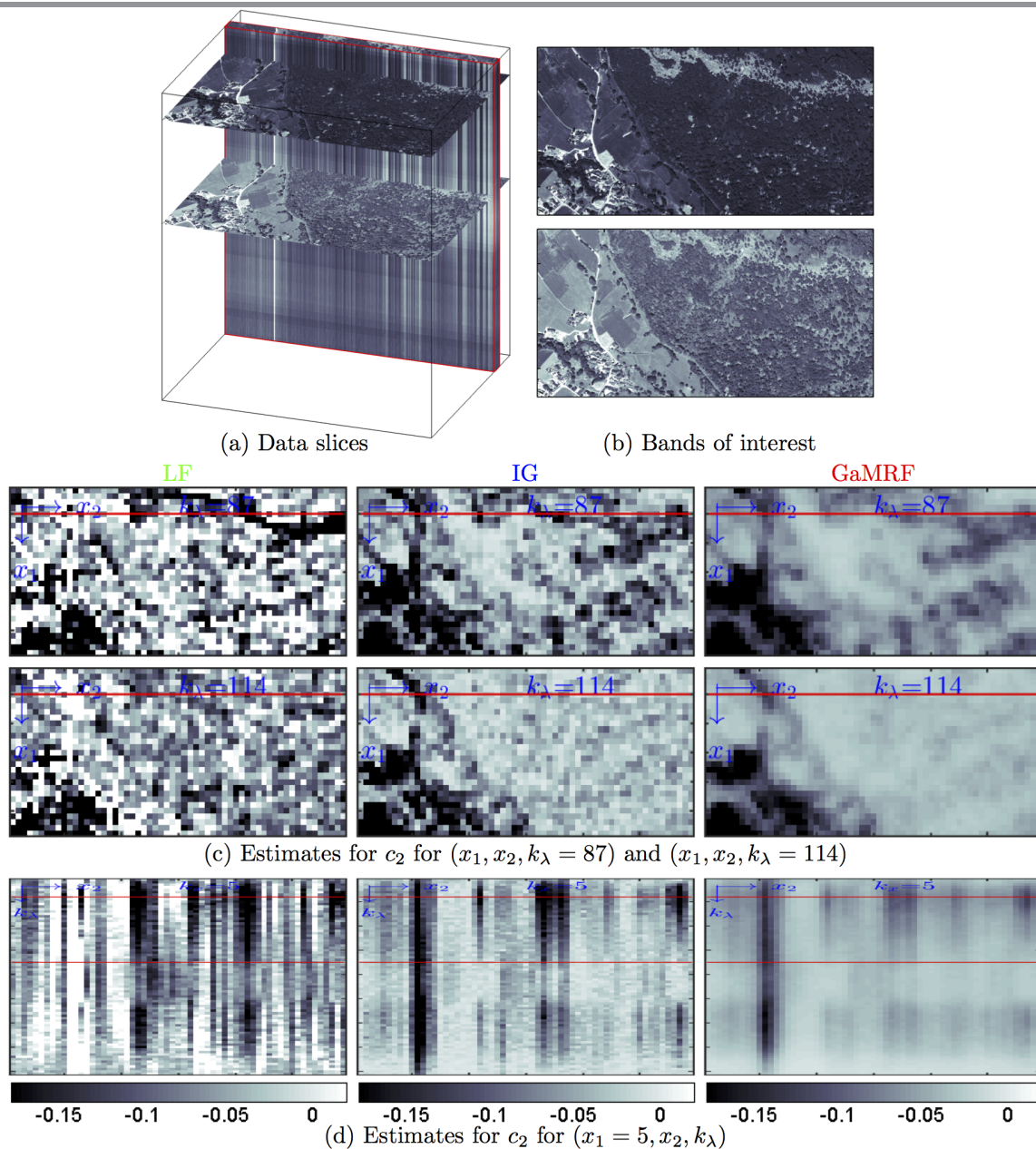


Figure 4: Multifractal analysis of a hyperspectral image (bands 80 – 160) from the Madonna project.

571 multivariate image by gamma Markov random field joint priors, accounting for the assump-  
 572 tion that multifractal properties evolve smoothly in privileged (temporal/spectral, spatial)  
 573 directions within the sequence of images and inducing regularization. Together, these two  
 574 ingredients lead to a Bayesian model for the multifractality parameters of multivariate im-

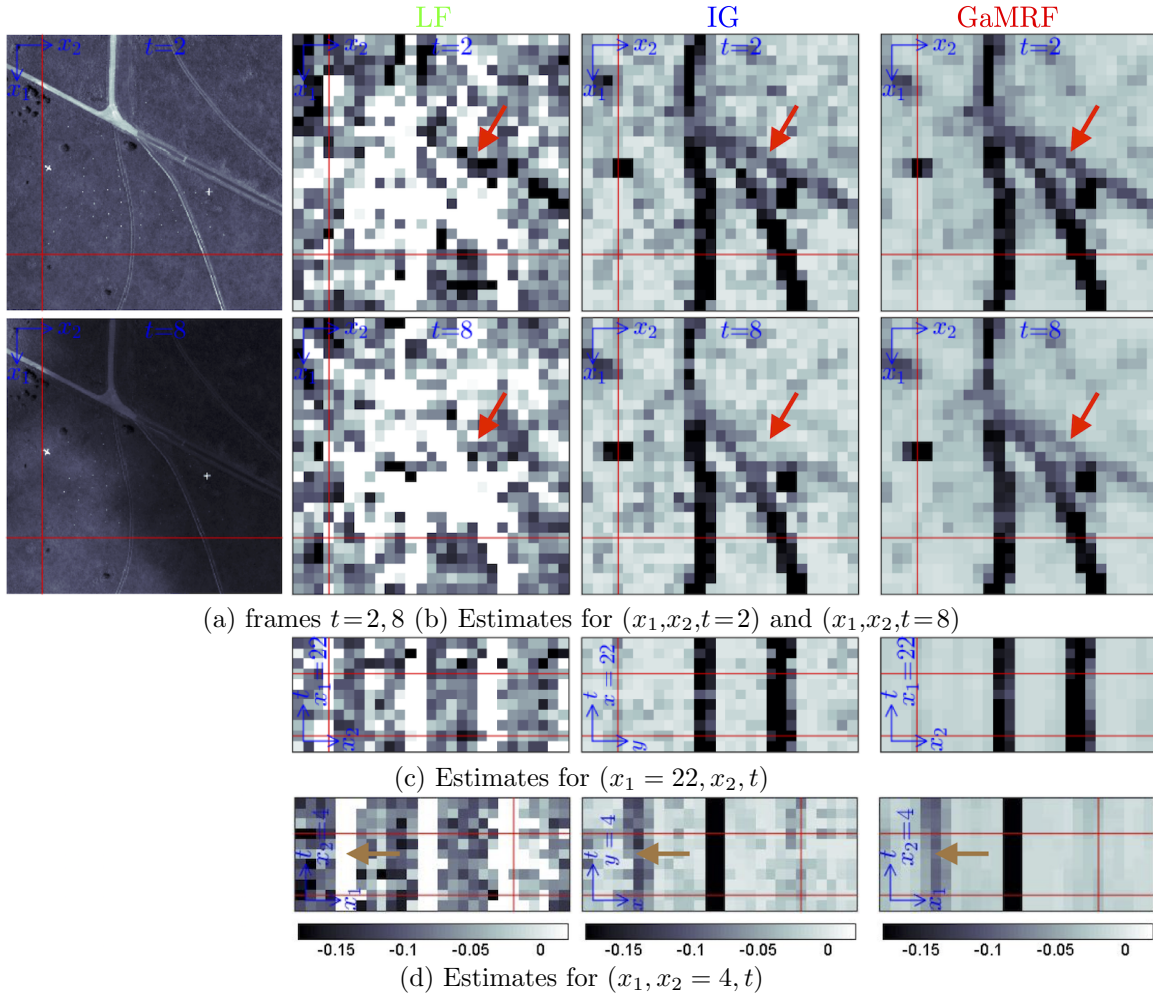


Figure 5: Multifractal analysis of a multi-temporal image.

575 ages for which the associated Bayesian estimators can be approximated efficiently using a  
 576 Gibbs sampler (without requiring any Metropolis-Hastings acceptance-reject move). To the  
 577 best of our knowledge, the method constitutes the first operational multifractal analysis tool  
 578 applicable to the joint analysis of multidimensional sets of images. Numerical experiments,  
 579 conducted on synthetic data with heterogeneous multifractal properties as well as on two real-  
 580 world hyperspectral and multi-temporal images, demonstrated the excellent performance of  
 581 the Bayesian joint estimator, which significantly outperformed previously existing (univariate)  
 582 methods. Moreover, the proposed Bayesian model results in a competitive computational cost,  
 583 of the order of 4 times the cost of linear regression based estimation. Future work will include  
 584 the incorporation of additional log-cumulants  $c_p$  in the statistical model and the investigation  
 585 of procedures for estimating the GaMRF regularization hyperparameters.

- 587 [1] P. ABRY, S. JAFFARD, AND H. WENDT, *When Van Gogh meets Mandelbrot: Multifractal classification*  
588 *of painting's texture*, Signal Proces., 93 (2013), pp. 554–572.
- 589 [2] V. V. ANH AND K. E. LUNNEY, *Parameter estimation of random fields with long-range dependence*,  
590 Math. Comput. Model., 21 (1995), pp. 67–77.
- 591 [3] J.-P. ANTOINE, R. MURENZI, P. VANDERGHEYNST, AND S. T. ALI, *Two-Dimensional Wavelets and their*  
592 *Relatives*, Cambridge University Press, 2004.
- 593 [4] A. ARNEODO, N. DECOSTER, P. KESTENER, AND S. G. ROUX, *A wavelet-based method for multifractal*  
594 *image analysis: from theoretical concepts to experimental applications*, in Adv. Imag. Electr. Phys.,  
595 vol. 126, Academic Press, 2003, pp. 1–98.
- 596 [5] C. L. BENHAMOU, S. POUPON, E. LESPESSAILLES, S. LOISEAU, R. JENNANE, V. SIROUX, W. J. OHLEY,  
597 AND L. POTHUAUD, *Fractal analysis of radiographic trabecular bone texture and bone mineral den-*  
598 *sity: two complementary parameters related to osteoporotic fractures*, J. Bone Miner. Res., 16 (2001),  
599 pp. 697–704.
- 600 [6] J. BERAN, *Statistics for Long-Memory Processes*, Chapman & Hall, New York, 1994.
- 601 [7] J. BESAG, *Statistical analysis of non-lattice data*, The Statistician, (1975), pp. 179–195.
- 602 [8] J. BRUNA, S. MALLAT, E. BACRY, AND J.-F. MUZY, *Intermittent process analysis with scattering mo-*  
603 *ments*, Ann. Stat., 43 (2015), pp. 323–351.
- 604 [9] B. CASTAING, Y. GAGNE, AND M. MARCHAND, *Log-similarity for turbulent flows?*, Physica D, 68 (1993),  
605 pp. 387–400, [https://doi.org/http://dx.doi.org/10.1016/0167-2789\(93\)90132-K](https://doi.org/http://dx.doi.org/10.1016/0167-2789(93)90132-K).
- 606 [10] P. CHAINAIS, *Infinitely divisible cascades to model the statistics of natural images*, IEEE T. Pattern Anal.  
607 Mach. Intell., 29 (2007), pp. 2105–2119.
- 608 [11] N. H. CHAN AND W. PALMA, *Estimation of long-memory time series models: A survey of different*  
609 *likelihood-based methods*, Adv. Econom., 20 (2006), pp. 89–121.
- 610 [12] C.-I. CHANG, Q. DU, T.-L. SUN, AND M. L. G. ALTHOUSE, *A joint band prioritization and band-*  
611 *decorrelation approach to band selection for hyperspectral image classification*, IEEE T. Geosc. Remote  
612 Sensing, 37 (1999), pp. 2631–2641.
- 613 [13] J. CODDINGTON, J. ELTON, D. ROCKMORE, AND Y. WANG, *Multifractal analysis and authentication of*  
614 *Jackson Pollock paintings*, in Proc. SPIE 6810, 2008, p. 68100F.
- 615 [14] S. COMBEXELLE AND H. WENDT, <https://www.irit.fr/~Herwig.Wendt/MVMFA.html>.
- 616 [15] S. COMBEXELLE, H. WENDT, Y. ALTMANN, J.-Y. TOURNERET, S. MCLAUGHLIN, AND P. ABRY, *A*  
617 *bayesian framework for the multifractal analysis of images using data augmentation and a whittle*  
618 *approximation*, in Proc. IEEE Int. Conf. Acoust., Speech, and Signal Process. (ICASSP), Shanghai,  
619 China, March 2016.
- 620 [16] S. COMBEXELLE, H. WENDT, Y. ALTMANN, J.-Y. TOURNERET, S. MCLAUGHLIN, AND P. ABRY,  
621 *Bayesian joint estimation of the multifractality parameter of image patches using gamma markov*  
622 *random field priors*, in Proc. IEEE Int. Conf. Image Proc. (ICIP), Phoenix, AZ, USA, September  
623 2016.
- 624 [17] S. COMBEXELLE, H. WENDT, N. DOBIGEON, J.-Y. TOURNERET, S. MCLAUGHLIN, AND P. ABRY,  
625 *Bayesian estimation of the multifractality parameter for image texture using a Whittle approximation*,  
626 IEEE T. Image Proces., 24 (2015), pp. 2540–2551.
- 627 [18] S. COMBEXELLE, H. WENDT, J.-Y. TOURNERET, P. ABRY, AND S. MCLAUGHLIN, *Bayesian multifractal*  
628 *analysis of multi-temporal images using smooth priors*, in Proc. IEEE Workshop Statistical Signal  
629 Proces. (SSP), Palma de Mallorca, Spain, June 2016.
- 630 [19] O. DIKMEN AND A. CEMGIL, *Gamma Markov random fields for audio source modeling*, IEEE T. Audio,  
631 Speech, and Language Proces., 18 (2010), pp. 589–601, <https://doi.org/10.1109/TASL.2009.2031778>.
- 632 [20] D. A. V. DYK AND X.-L. MENG, *The art of data augmentation*, J. of Comput. and Graphical Stat., 10  
633 (2001), pp. pp. 1–50.
- 634 [21] M. FUENTESE, *Approximate likelihood for large irregularly spaced spatial data*, J. Am. Statist. Assoc., 102  
635 (2007), pp. 321–331.
- 636 [22] N. R. GOODMAN, *Statistical analysis based on a certain multivariate complex Gaussian distribution (an*  
637 *introduction)*, Ann. Math. Stat., 34 (1963), pp. pp. 152–177.
- 638 [23] T. C. HALSEY, M. H. JENSEN, L. P. KADANOFF, I. PROCACCIA, AND B. I. SHRAIMAN, *Fractal measures*

- 639 *and their singularities: The characterization of strange sets*, Phys. Rev. A, 33 (1986), pp. 1141–1151,  
640 <https://doi.org/10.1103/PhysRevA.33.1141>.
- 641 [24] R. M. HARALICK, *Statistical and structural approaches to texture*, Proc. of the IEEE, 67 (1979), pp. 786–  
642 804.
- 643 [25] G. E. HINTON, *Training products of experts by minimizing contrastive divergence*, Neural computation,  
644 14 (2002), pp. 1771–1800.
- 645 [26] S. JAFFARD, *Wavelet techniques in multifractal analysis*, in Fractal Geometry and Applications: A Ju-  
646 bilee of Benoît Mandelbrot, Proc. Symp. Pure Math., M. Lapidus and M. van Frankenhuysen, eds.,  
647 vol. 72(2), AMS, 2004, pp. 91–152.
- 648 [27] S. JAFFARD, P. ABRY, AND H. WENDT, *Irregularities and scaling in signal and image processing: Mul-  
649 tifractal analysis*, in Benoit Mandelbrot: A Life in Many Dimensions, M. Frame and N. Cohen, eds.,  
650 World scientific publishing, Singapore, 2015, pp. 31–116.
- 651 [28] S. JAFFARD, S. SEURET, H. WENDT, R. LEONARDUZZI, S. ROUX, AND P. ABRY, *Multivariate multifractal  
652 analysis*, Applied and Computational Harmonic Analysis, (2018). in press.
- 653 [29] H. JI, X. YANG, H. LING, AND Y. XU, *Wavelet domain multifractal analysis for static and dynamic  
654 texture classification*, IEEE T. Image Proces., 22 (2013), pp. 286–299.
- 655 [30] C. R. JOHNSON, P. MESSIER, W. SETHARES, A. KLEIN, C. BROWN, A. DO, P. KLAUSMEYER,  
656 P. ABRY, S. JAFFARD, H. WENDT, S. ROUX, N. PUSTELNIK, N. VAN NOORD, L. VAN DER MAATEN,  
657 E. POTSMAN, J. CODDINGTON, L. DAFFNER, H. MURATA, H. WILHELM, S. WOOD, AND M. MESSIER,  
658 *Pursuing automated classification of historic photographic papers from raking light photomicrographs*,  
659 J. Amer. Inst. Conserv., 53 (2014), pp. 159–170.
- 660 [31] P. KESTENER, J. LINA, P. SAINT-JEAN, AND A. ARNEODO, *Wavelet-based multifractal formalism to  
661 assist in diagnosis in digitized mammograms*, Image Analysis and Stereology, 20 (2001), pp. 169–175.
- 662 [32] J. LÉVY-VÉHEL, P. MIGNOT, AND J. BERROIR, *Multifractals, texture and image analysis*, in Proc. IEEE  
663 Conf. Comp. Vis. Pattern Recognition (CVPR), Champaign, IL, USA, June 1992, pp. 661–664.
- 664 [33] R. LOPES AND N. BETROUNI, *Fractal and multifractal analysis: A review*, Medical Image Analysis, 13  
665 (2009), pp. 634–649.
- 666 [34] S. LOVEJOY AND D. SCHERTZER, *The weather and climate: emergent laws and multifractal cascades*,  
667 Cambridge University Press, 2013.
- 668 [35] T. LUX, *Higher dimensional multifractal processes: A GMM approach*, J. Business & Economic Stat., 26  
669 (2007), pp. 194–210.
- 670 [36] S. MALLAT, *A Wavelet Tour of Signal Processing*, Academic Press, 3rd ed., 2008.
- 671 [37] B. B. MANDELBROT, *Intermittent turbulence in self-similar cascades: divergence of high moments  
672 and dimension of the carrier*, J. Fluid Mech., 62 (1974), pp. 331–358, [https://doi.org/10.1017/  
673 S0022112074000711](https://doi.org/10.1017/S0022112074000711).
- 674 [38] C. MENEVEAU, K. SREENIVASAN, P. KAILASNATH, AND M. FAN, *Joint multifractal measures: Theory  
675 and applications to turbulence*, Phys. Rev. A, 41 (1990), p. 894.
- 676 [39] E. MOULINES, F. ROUEFF, AND M. TAQQU, *A wavelet Whittle estimator of the memory parameter of a  
677 nonstationary Gaussian time series*, Ann. Stat., (2008), pp. 1925–1956.
- 678 [40] M. PEREYRA, N. WHITELEY, C. ANDRIEU, AND J.-Y. TOURNERET, *Maximum marginal likelihood  
679 estimation of the granularity coefficient of a Potts-Markov random field within an MCMC algo-  
680 rithm*, in Proc. IEEE Workshop on Statistical Signal Proces. (SSP), June 2014, pp. 121–124,  
681 <https://doi.org/10.1109/SSP.2014.6884590>.
- 682 [41] L. PONSON, D. BONAMY, H. AURADOU, G. MOURROT, S. MOREL, E. BOUCHAUD, C. GUILLOT, AND  
683 J. HULIN, *Anisotropic self-affine properties of experimental fracture surface*, J. Fracture, 140 (2006),  
684 pp. 27–36.
- 685 [42] J. PRATS-MONTALBN, A. DE JUAN, AND A. FERRER, *Multivariate image analysis: A review with applica-  
686 tions*, Chemometrics and Intelligent Laboratory Systems, 107 (2011), pp. 1–23, [https://doi.org/http:  
687 //dx.doi.org/10.1016/j.chemolab.2011.03.002](https://doi.org/http://dx.doi.org/10.1016/j.chemolab.2011.03.002).
- 688 [43] T. S. RAO AND R. CHANDLER, *A frequency domain approach for estimating parameters in point process  
689 models*, in Athens Conf. Applied Probability and Time Series Analysis, Springer, 1996, pp. 392–405.
- 690 [44] R. H. RIEDI, *Multifractal processes*, in Theory and applications of long range dependence, P. Doukhan,  
691 G. Oppenheim, and M. Taqqu, eds., Birkhäuser, 2003, pp. 625–717.
- 692 [45] L. RISSER, T. VINCENT, F. FORBES, J. IDIER, AND P. CIUCIU, *Min-max extrapolation scheme for fast*

- 693 *estimation of 3d potts field partition functions. application to the joint detection-estimation of brain*  
 694 *activity in fMRI*, J. Signal Proces. Syst., 65 (2011), pp. 325–338.
- 695 [46] C. P. ROBERT AND G. CASELLA, *Monte Carlo Statistical Methods*, Springer, New York, USA, 2005.
- 696 [47] R. ROBERT AND V. VARGAS, *Gaussian multiplicative chaos revisited*, Ann. Proba., 38 (2010), pp. 605–631.
- 697 [48] S. G. ROUX, A. ARNEODO, AND N. DECOSTER, *A wavelet-based method for multifractal image analysis.*  
 698 *III. Applications to high-resolution satellite images of cloud structure*, Eur. Phys. J. B, 15 (2000),  
 699 pp. 765–786.
- 700 [49] F. SCHMITT, D. SCHERTZER, S. LOVEJOY, AND Y. BRUNET, *Multifractal temperature and flux of tem-*  
 701 *perature variance in fully developed turbulence*, Europhys. Lett., 34 (1996), p. 195.
- 702 [50] F. G. SCHMITT AND L. SEURONT, *Multifractal random walk in copepod behavior*, Physica A, 301 (2001),  
 703 pp. 375–396.
- 704 [51] D. SHEEREN, M. FAUVEL, S. LADET, A. JACQUIN, G. BERTONI, AND A. GIBON, *Mapping ash tree*  
 705 *colonization in an agricultural mountain landscape: Investigating the potential of hyperspectral im-*  
 706 *agery*, in Proc. IEEE Int. Conf. Geosci. Remote Sens. (IGARSS), Vancouver, Canada, July 2011,  
 707 pp. 3672–3675.
- 708 [52] M. A. TANNER AND W. H. WONG, *The calculation of posterior distributions by data augmentation*, J.  
 709 Am. Stat. Ass., 82 (1987), pp. pp. 528–540.
- 710 [53] C. VACAR, J.-F. GIOVANNELLI, AND Y. BERTHOUMIEU, *Bayesian texture classification from indirect*  
 711 *observations using fast sampling*, IEEE Transactions on Signal Processing, 64 (2016), pp. 146–159.
- 712 [54] H. WENDT, P. ABRY, AND S. JAFFARD, *Bootstrap for empirical multifractal analysis*, IEEE Signal Proces.  
 713 Mag., 24 (2007), pp. 38–48.
- 714 [55] H. WENDT, P. ABRY, S. JAFFARD, H. JI, AND Z. SHEN, *Wavelet leader multifractal analysis for texture*  
 715 *classification*, in Proc. IEEE Int. Conf. Image Proces. (ICIP), Cairo, Egypt, Nov. 2009.
- 716 [56] H. WENDT, S. JAFFARD, AND P. ABRY, *Multifractal analysis of self-similar processes*, in Proc. IEEE  
 717 Workshop on Statistical Signal Proces. (SSP), Ann Arbor, MI, USA, Aug. 2012, pp. 69–72, <https://doi.org/10.1109/SSP.2012.6319798>.  
 718
- 719 [57] H. WENDT, R. LEONARDUZZI, P. ABRY, S. ROUX, S. JAFFARD, AND S. SEURET, *Assessing cross-*  
 720 *dependencies using bivariate multifractal analysis*, in IEEE Int. Conf. Acoust., Speech, and Signal  
 721 Proces. (ICASSP), Calgary, Canada, April 2018.
- 722 [58] H. WENDT, S. G. ROUX, S. JAFFARD, AND P. ABRY, *Wavelet leaders and bootstrap for multifractal*  
 723 *analysis of images*, Signal Proces., 89 (2009), pp. 1100–1114, [https://doi.org/http://dx.doi.org/10.](https://doi.org/http://dx.doi.org/10.1016/j.sigpro.2008.12.015)  
 724 [1016/j.sigpro.2008.12.015](https://doi.org/http://dx.doi.org/10.1016/j.sigpro.2008.12.015).
- 725 [59] P. WHITTLE, *On stationary processes in the plane*, Biometrika, 41 (1954), pp. 434–449.
- 726 [60] G. WORNELL AND A. V. OPPENHEIM, *Estimation of fractal signals from noisy measurements using*  
 727 *wavelets*, IEEE T. Signal Proces., 40 (1992), pp. 611–623.
- 728 [61] Y. XU, X. YANG, H. LING, AND H. JI, *A new texture descriptor using multifractal analysis in multi-*  
 729 *orientation wavelet pyramid*, in Proc. IEEE Conf. Comp. Vis. Pattern Recognition (CVPR), San  
 730 Francisco, CA, USA, June 2010, pp. 161–168.